J Adv Ceram

Research Article

Hierarchically structured aluminum borate whisker aerogel via sol–gel method and *in-situ* reaction

Xin Tao[1], Liangying Tang[2], Yuqi Zhao[1], Fangyu Zhao[3], Ziwei Xiang[3], Xinyue He[1], Mingchao Wang[1,✉]

Cite this article: Tao X, Tang L, Zhao Y, et al. *J Adv Ceram* 2026, **15**(4): 9221270. https://doi.org/10.26599/JAC.2026.9221270

ABSTRACT: Ultralight, thermally insulating, and temperature-resistant inorganic aerogels, including particulate and fibrous aerogels, serve as excellent thermal protection materials and hold significant applications in aerospace, energy, and environmental engineering. In this work, hierarchical aluminum borate whisker (ABOw) aerogels were prepared via a sol–gel process, followed by freeze-drying and high-temperature *in-situ* reaction, in which ABOw uniformly grows within the matrix, interspersed with either mullite fibers covered by ABOw or rod-like ABOw assemblies. The size of ABOw within the matrix and the phase transformation temperature ($Al_4B_2O_9 \rightarrow Al_{18}B_4O_{33}$) decrease with increasing Al/B ratio. ABOw growth follows the V–S–L mechanism: Within the matrix, whiskers nucleate uniformly around alumina particles and then grow; in contrast, whiskers on the fiber surface nucleate heterogeneously on preferentially oriented mullite grains, grow in clusters, and gradually merge into a single whisker of increasing length. The density of the ABOw aerogel ranges from 0.173 to 0.243 g/cm^3, which decreases with increasing calcination temperature and decreasing Al/B ratio. The thermal conductivity lies between 0.0560 and 0.0873 W/(m·K) and increases with increasing calcination temperature. The ABOw aerogels calcined at 1200 °C have a compressive strength of 97.8–214.3 kPa, and the main failure modes are matrix fracture and interfacial cracking. The aerogel with an Al/B ratio of 2 : 1 exhibits a linear shrinkage of less than 5% without obvious welding phenomena after high-temperature heat treatment (1400 °C/20 h, 1500 °C/2 h). This high-temperature resistant, lightweight, and thermally insulating ABOw aerogel is an excellent thermal protection material and is also suitable for high-temperature filtration, adsorption, and catalysis.

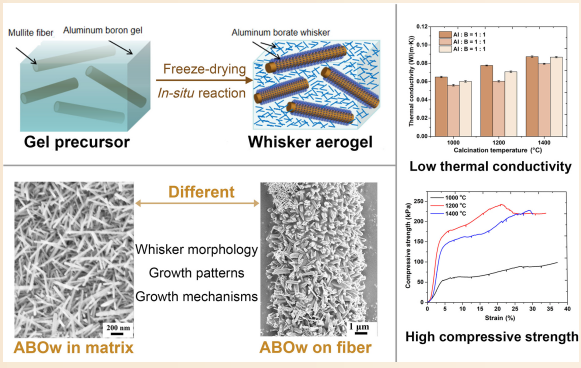

KEYWORDS: aerogel; aluminum borate whisker; sol–gel method; *in-situ* reaction; whisker growth mechanism

1 Introduction

With the rapid development of hypersonic aircraft and space shuttles, there is an increasing demand for high-temperature thermal-insulating refractories and higher performance requirements. Inorganic aerogels, as ultralight solid materials that combine extremely low density with excellent thermal insulation and high-temperature resistance, have become a key material addressing core challenges across multiple fields [1–4]. Aerogels are mainly divided into two categories: particulate aerogels and fibrous aerogels. Particulate aerogels are composed of nanoscale primary aerogel particles, and they always exhibit high brittleness and fragility [5–7]. The preparation of particulate aerogels primarily relies on the sol–gel method, which involves hydrolysis and gelation, followed by appropriate drying techniques to remove the solvent while completely preserving the porous network structure. Fibrous aerogels are composed of a three-dimensional network of interwoven nanoscale ceramic fibers, which exhibit exceptional flexibility and high toughness because the fibrous network effectively dissipates and absorbs stress [8–10]. The production of fibrous aerogels typically requires a two-step method, in which nanofibers are first prepared through electrospinning, solution blow-spinning, and chemical vapor deposition, followed by shaping them into specific structures, making the overall process relatively complex. It is evident that the nanoscale units within aerogels fundamentally influence the material's properties. If a three-dimensional porous structure is constructed using nanoscale whiskers as the building blocks, what specific structural and performance characteristics would distinguish such whisker aerogels?

Aluminum borate ($Al_4B_2O_9$ and $Al_{18}B_4O_{33}$) ceramics, which have high compressive strength, high elastic modulus, and excellent thermal and corrosion resistance, are widely used in high-temperature thermal protection fields [11,12]. The crystal

[1] College of Science, Civil Aviation University of China, Tianjin 300300, China. [2] Aviation Engineering Institute, Civil Aviation University of China, Tianjin 300300, China. [3] Department of Safety Engineering, Civil Aviation University of China, Tianjin 300300, China.

✉ Corresponding author. E-mail: mingchaowang0@163.com

Received: December 8, 2025; Revised: January 26, 2026; Accepted: February 20, 2026

structure of aluminum borate belongs to the orthorhombic crystal system, exhibiting significant anisotropy. The binding energy of atoms along the *c*-axis is lower, and the growth rate in this direction is significantly higher than that in other directions, thus favoring the formation of whiskers. The aluminum borate whiskers (ABOw) possess intrinsic high strength and high modulus, which can interlock and form a three-dimensional, highly porous structure, holding promise for the development of a novel whisker aerogel. In addition, the aspect ratio and dimensions of the whiskers can be precisely controlled by adjusting the Al/B ratio in the raw material and heat treatment temperature [13,14], enabling the creation of aerogel materials with highly tunable pore structures and properties.

Although to the best of the author's knowledge, there is no reported ABOw aerogel, ABOw has been widely used in the preparation of dense/porous ceramic materials, fiber-whisker composite porous ceramics, and as a reinforcement agent in composite materials. Aluminum borate ceramics are typically synthesized using boric oxide and aluminum oxide as raw materials, which are shaped and subsequently fired at high temperatures. These ceramics exhibit excellent heat resistance (above 1400 °C) and outstanding mechanical properties. However, this method generally results in limited porosity, and the whiskers tend to grow in a clustered pattern nucleating from alumina particles, leading to poor uniformity and a low aspect ratio [15–17]. Fiber-whisker composite porous materials are fabricated by mixing fibers with aluminum and boron sources used for synthesizing ABOw. This process utilizes the porous structure formed by the fibers, with the fiber surfaces serving as growth substrates for the *in-situ* formation of whiskers. The resulting material exhibits a hierarchical porous structure, comprising macropores between fibers and micropores between whiskers, and generally demonstrates both high porosity and enhanced mechanical strength [18–20]. In whisker-reinforced composites, boron and aluminum sources are incorporated into the matrix, followed by heat treatment to generate whisker reinforcement *in-situ*. The whiskers effectively enhance the strength, fracture toughness, and wear resistance by transferring loads and impeding crack propagation [21,22]. Therefore, the utilization of refined aluminum and boron sources along with precise control over the porous network formation is crucial for preparing ABOw aerogels. In this study, boric acid and aluminum sol were used as raw materials to first synthesize a boron–aluminum sol. Subsequently, a three-dimensional network was constructed through a sol–gel method followed by freeze-drying. Finally, *in-situ* growth of ABOw was achieved via high-temperature calcination.

However, compared with commonly used silica or alumina sols in aerogel preparation, boron–aluminum sol presents two critical drawbacks, which explain the current absence of studies on synthesizing aluminum borate aerogels via a sol–gel method. First, the central atoms (B, Al) in boron–aluminum sol exhibit high electrophilicity, making them particularly susceptible to nucleophilic attack by water molecules [23,24]. This leads to rapid gelation, severely limiting the operability during the aerogel shaping process. Second, the boron–aluminum gel network features relatively large distances between cross-linking points, resulting in a loose structure. Additionally, some B–O bonds exhibit coordinate bond characteristics, making the aerogel network highly prone to collapse during drying [25–27]. To address these challenges, this study developed a low-activity boron–aluminum sol by combining two types of aluminum sols with differing cross-linking reactivities, thereby achieving controlled gelation. Furthermore, mullite fibers were introduced into the aerogel network as a secondary aluminum source. This approach not only enhances the network strength during gelation and drying but also enables the fibers to transform into a columnar assembly of aluminum borate whiskers at high temperatures, ultimately forming a hierarchical ABOw aerogel.

In this work, hierarchically structured ABOw aerogels were prepared by the sol–gel method and *in-situ* reaction. The gelation process of the modified boron–aluminum sol was meticulously characterized. The influence of the Al/B ratio and calcination temperature on whisker morphology was systematically investigated. A comparative analysis was conducted on the growth of ABOw within the matrix and on the mullite fiber surfaces, elucidating the distinct whisker growth patterns and mechanisms. The pore structure, phase evolution, mechanical strength, thermal conductivity, and temperature resistance of the ABOw aerogels were thoroughly characterized. The influencing mechanisms of whisker morphology and pore structure on strength and thermal conductivity were analyzed.

2 Materials and methods

2.1 Materials

To prepare the ABOw aerogel, boron oxide (B_2O_3, analytical reagent (AR), Shanghai Aladdin Biochemical Technology Co., Ltd.) was used as the boron source. Aluminum sol (denoted as Sol-A) prepared from nanoalumina colloidal powder (JHALH-15, Jinghuo Technology Glass Co., Ltd., China) was used as the aluminum source, and the main technical parameters are listed in Table 1. The preparation method of Sol-A is as follows: Colloidal powder is slowly added to water under magnetic stirring for more than 2 h until a stable sol is formed, and then it is allowed to stand for 24 h before use. A commercially available acidic aluminum sol (Jinghuo Technology Glass Co., Ltd., China), prepared by the salt-aluminum method, was used to regulate the gelation process of the precursor, which is denoted as Sol-B. Its detailed parameters are listed in Table 2.

Chopped polycrystalline mullite fibers were used as the second aluminum source in the porous material, which was obtained from commercially available mullite fiber felt (99.5%, Zhejiang Hongda Crystal Fiber Co., Ltd., China) by cutting, cleaning, deslagging, drying, and dispersing. The X-ray diffraction (XRD)

Table 1 Main technical parameters of the nanoalumina colloidal powder

Name	Composition	Particle shape	Preparable sol solid content (wt%)	pH (30 wt%)	Specific surface area (m^2/g)	Particle size (nm)
Nanoalumina powder	AlOOH	Rod-like or feather-like	1–30	4.51	250±10	10–50

Table 2 Main technical parameters of aluminum Sol-B

Name	Solid content (wt%)	Aluminum/chlorine ratio	Density (g/cm^3)	pH	Iron content (%)
Aluminum sol	30	1.2–1.4	1.3–1.5	2.89	< 0.2%

patterns, morphology, elemental mapping, energy dispersive spectroscopy (EDS) analysis, and elemental composition are shown in Fig. S1 in the Electronic Supplementary Material (ESM). The fibers exhibit good uniformity, with aluminum, silicon, and oxygen distributed evenly. The molar ratio of aluminum to silicon is approximately 3 : 1, which aligns with the stoichiometry of Al_3S_2 ($3Al_2O_3{\cdot}2SiO_2$). A 10% sodium dodecylbenzenesulfonate (SDBS) solution was used as the dispersant, and n-octanol was used as the defoamer. Both of them were of analytical grade and purchased from Shanghai Aladdin Biochemical Technology Co., Ltd.

2.2 Preparation process

The preparation process of the ABOw aerogel is shown in Fig. 1. The first step is preparing the mixed sol: First, boron oxide is mixed with water to form a 12 wt% solution by heating at 100 °C and continuously magnetically stirring (400 r/min); then, mullite fibers are added in small batches (the mass ratio of mullite fibers to the total mass of boron oxide and aluminum oxide in the system is 1 : 6), the dispersant (10% SDBS) is added at a dosage of 1% of the fiber mass, and the defoamer (n-octanol, 0.2 g) is added, followed by continuous stirring for 30 min. After that, the prepared Sol-A is slowly added and stirred continuously for 15 min. Finally, Sol-B is added drop by drop (the dosage is 2% of the mass of the boron oxide solution) and stirred until the viscosity of the mixed solution increases. After that, the prepared mixed sol was poured into a mold for casting (squares with a side length of 20 mm), sealed with plastic wrap, and aged at room temperature for 24 h for gelation and aging of the gel network. Subsequently, the sample was demolded and frozen in an ultralow temperature refrigerator at −50 °C for 12 h; then, it was transferred to a freeze dryer and freeze-dried for 24 h under the conditions of a pressure of 10–20 Pa and a cold trap temperature of −50 °C. Finally, the sample was sintered in a high-temperature furnace in a sealed environment for *in-situ* reaction synthesis of ABOw, with a holding time of 2 h, and the sintering temperatures were 1000, 1200, and 1400 °C. In this study, three different Al/B ratios were adopted to investigate their effects on whisker growth and material properties: 1 : 1, 1 : 2, and 2 : 1.

2.3 Characterization and testing

A scanning electron microscope (SEM; Tescan Mira Lms, Czech Republic) was used for microstructural and elemental analyses. A transmission electron microscope (TEM; FEI Tecnai F20, Japan) equipped with an energy dispersive spectrometer and selected area electron diffraction (SAED) was used to characterize the whiskers. The phase composition of the composite was analyzed via an X-ray diffractometer (XRD; D/Max-2500 Rigaku, Japan) with filtered Cu Kα radiation. The pore size distribution and specific surface area of the porous material were tested using an automatic specific surface area and porosity analyzer (Micromeritics ASAP 2460, USA) based on Brunauer–Emmet–Teller (BET) theory. Thermogravimetric and differential scanning calorimetry (TG/DSC) analysis was performed using a simultaneous thermal analyzer (STA-449C, Netzsch, Germany) with a heating speed of 10 °C/min in an air atmosphere. The molecular structure was identified by Fourier transform infrared spectroscopy (FTIR; Nicolet iS5, Thermo Scientific, USA) in the wavenumber range of 4000–400 cm^{-1}, in which the samples were ground with dried potassium bromide (KBr) powder and pressed into a disc. The surface element composition and valence state of the samples were tested by an X-ray photoelectron spectrometer (XPS; Thermo Scientific ESCALAB 250Xi), and Avantage software was used for the data processing. The density was obtained by dividing the mass by the volume, and each group of samples tested ten blocks to obtain an average value. The thermal conductivity was tested by a Hot Disk TPS 2500 thermal constant analyzer at room temperature, 200, 400, and 600 °C. The result was the average of the measurements at nine locations on the samples. The integrating sphere reflectivity of the ABOw aerogel in the wavenumber range of 4000–400 cm^{-1} was measured by a Fourier transform infrared spectrometer (Nicolet IS50, Thermo Fisher, USA), and the spectral emissivity was obtained from the measured reflectance based on the relation for materials, $\varepsilon = A = 1 - R - T$, where ε, A, R, and T are the emissivity, absorptivity, reflectivity, and transmissivity, respectively. For a perfect opaque body, the total emissivity ε_t can be derived from the reflectance spectrum according to Eqs. (1) and (2):

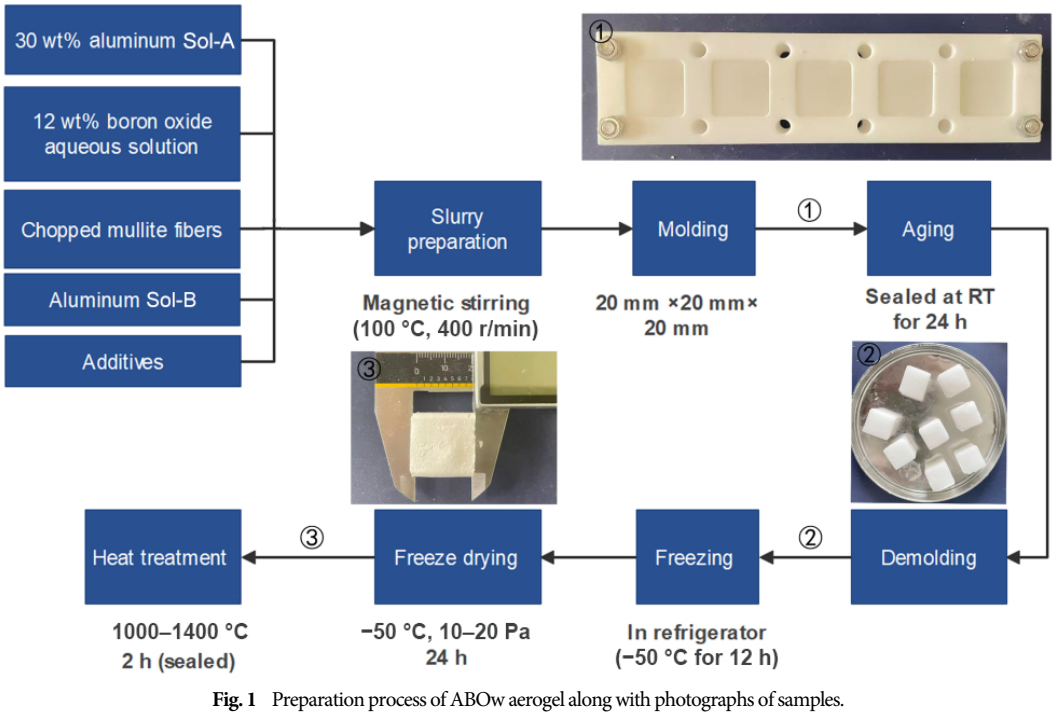

Fig. 1 Preparation process of ABOw aerogel along with photographs of samples.

$$\varepsilon_t = \frac{\int_{\lambda_1}^{\lambda_2} (1 - R(\lambda)) P_B(\lambda) d\lambda}{\int_{\lambda_1}^{\lambda_2} P_B(\lambda) d\lambda} \quad (1)$$

$$P_B(\lambda) = \frac{C_1}{\lambda^5 \left(\exp \frac{C_2}{\lambda T} - 1 \right)} \quad (2)$$

where λ is the wavelength, $R(\lambda)$ is the reflectance, and $P_B(\lambda)$ is given by Planck's law, $C_1 = 3.743 \times 10^{-16}$ W·m^2, $C_2 = 1.4387 \times 10^{-2}$ mK.

An electronic universal mechanical testing machine (CSS-44001, Changchun Testing Machine Research Institute, China) was used to measure the compressive strength of the samples at a displacement rate of 0.2 mm/min at room temperature. The tests were conducted in accordance with GB/T 1964-2023 using cubic samples with a side length of 20 mm, with six repeated measurements for each sample. The compressive strength of the samples was defined as the stress at 10% strain, and the Young's modulus was calculated as the slope of the linear region in the compressive stress–strain curves. To test the thermal resistance of the ABOw aerogel, the aerogel calcined at 1000 °C was treated in a high-temperature electric furnace with heat preservation at 1400 °C for 20 h and at 1500 °C for 2 h, followed by morphological and phase characterization.

3 Results and discussion

3.1 Formation process of ABOw aerogel

The sol–gel process is the first critical step in the formation of aerogels, with the key lying in controlling the reaction and gelation process between the B_2O_3 solution and the aluminum sol. In this experiment, two types of aluminum sols were used as the main aluminum source (Sol-A) and the gelation accelerator (Sol-B).

Figure 2(a) shows the particle size distribution curve of Sol-A. The majority of particles (98.2%) are concentrated at approximately 29.52 nm, indicating a relatively uniform particle size distribution. A small proportion of particles (1.8%) have a size of 110.5 nm, representing a minor proportion of larger particles. Figure 2(b) is a zeta potential distribution diagram of Sol-A. The zeta potential is 35.3 mV, and its high absolute value indicates excellent dispersion stability of the particles in the system. The zeta potential deviation is 7.37 mV, which reflects the uniform surface charge characteristics of the particles in the system. The conductivity of the sol is 0.0306 mS/cm. The low-ionic environment prevents the compression of the electric double layer around the particles, collectively demonstrating the excellent electrostatic stability of this sol. The XRD pattern of the nanoalumina powders used for the preparation of Sol-A is shown in Fig. 2(c), and the diffraction peaks align well with the standard pattern of boehmite ($Al_2(OOH)_2$, PDF#05-0190). The weak diffraction peak intensity and peak broadening indicate a small crystallite size and a moderate degree of crystallinity. The TEM image of the nanoalumina powder is presented in Fig. 2(d), showing a relatively uniform feather-like structure with a high specific surface area. The SAED pattern (Fig. 2(h)) displays diffuse ring-like diffraction, which indicates low crystallinity of the material and may also be related to the size effect of microcrystals.

Figure 2(e) displays photographs of Sol-A and Sol-B with a solid content of 30%. Sol-A presents a milky white, opaque appearance, while Sol-B appears as a transparent liquid, indicating that the particle size in Sol-B is smaller or it has better dispersibility, resulting in a weaker scattering effect on light. To compare the gelation process of the two types of sols after mixing with a B_2O_3 solution, Figs. 2(f) and 2(g) show photographs of B_2O_3 solution (10 wt%) at different time points after adding equal amounts of Sol-A and Sol-B, respectively. The experimental conditions were heating at 100 °C and magnetic stirring at 400 r/min. B_2O_3 forms boric acid (H_3BO_3) when dissolved in water ($B_2O_3 + 3H_2O = 2H_3BO_3$). H_3BO_3 acts as a Lewis acid in aqueous solution and combines with water molecules to form $B(OH)_4^-$. Under heating conditions, it adsorbs onto the surface of positively charged aluminum sol particles, neutralizing their charges and making it easier for the particles to approach. As the colloidal stability is disrupted and B–O–Al chemical bonds begin to form, the entire system gradually transforms into a three-dimensional network structure (gel) that traps water molecules inside [28,29]. When Sol-B was mixed with H_3BO_3, the system gelled rapidly: Its fluidity had decreased by 15 s, and it had completely solidified by 47 s. The magnetic stir bar was fully immobilized and could not rotate, indicating the formation of a

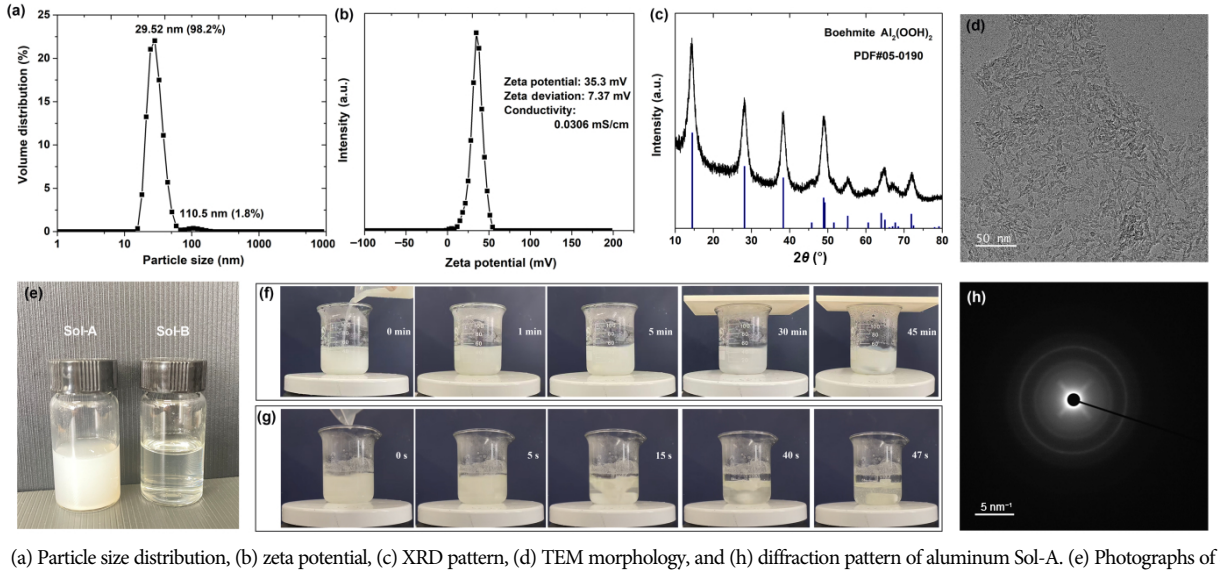

Fig. 2 (a) Particle size distribution, (b) zeta potential, (c) XRD pattern, (d) TEM morphology, and (h) diffraction pattern of aluminum Sol-A. (e) Photographs of Sol-A and Sol-B (30 wt%). Gelation process of (f) Sol-A and (g) Sol-B mixed with an aqueous solution of boron oxide (10 wt%) (conditions: 100 °C, 400 r/min magnetic stirring).

strong gel network. In contrast, the gelation of Sol-A was much slower: A decrease in fluidity was observed only at 30 min, with a gel layer forming on the surface; the upper layer had completely gelled by 45 min, while the magnetic stir bar continued to rotate in the lower layer. The possible reasons are as follows: Sol-A is prepared using nanofeather-like alumina powder, and the pH value (4.51) is higher than that of Sol-B (2.89). Meanwhile, the boehmite particles in Sol-A are significantly larger than the groups such as $(Al(H_2O)_6)^{3+}$ and $(AlO_4Al_{12}(OH)_{24}(H_2O)_{12})^{7+}$ in Sol-B, of which the XRD pattern indicates an amorphous structure (Fig. S2 in the ESM). Therefore, the reaction with boric acid and the gelation process were delayed, providing working time for the shaping process of the porous materials.

Schematic diagrams of the sample microstructure after gelation, freeze-drying, and calcination are illustrated in Fig. 3(a). The network structure of the gelled sample is strengthened after aging, and a gel precursor is formed after demolding, which contains a large amount of free water in its gel network, with mullite fibers uniformly distributed within it. After freeze-drying, an aerogel precursor is formed, which contains a large number of nanoscale pores, and the surface of the mullite fibers is also coated with a layer of boron–aluminum oxide. Finally, after calcination at high temperature, the boron source reacts with the aluminum source, and ABOw grows both inside the matrix and on the surface of the mullite fibers. When the calcination temperature exceeds 1200 °C, the mullite fibers covered with surface whiskers gradually transform into a columnar ABOw assembly, forming a hierarchically structured ABOw aerogel.

The SEM images of the ABOw aerogel calcined at 1000 °C are shown in Figs. 3(b)–3(e), in which a large number of nanoscale whiskers interweave with one another, forming a highly porous aerogel network that serves as the matrix. Meanwhile, mullite fibers also exhibit whisker growth on their surfaces, which are embedded within the matrix. The morphology and dimensions of the whiskers on the mullite fiber surfaces distinctly differ from those within the matrix. The low-magnification optical micrograph (Fig. S3 in the ESM) shows that the mullite fibers are distributed relatively uniformly, which can be attributed to the good fluidity of the aluminum–boron sol before setting and the electrostatic stabilization mechanism provided by the dispersant, which allows the chopped mullite fibers to be uniformly distributed within the sol. The SEM images of the aerogel calcined at 1400 °C are shown in Figs. 3(f)–3(i). As the calcination temperature increased from 1000 to 1400 °C, the whiskers exhibited notable growth in dimensions while retaining the three-dimensional architecture where ABOw assembled fibers interpenetrate a whisker-populated matrix without distinct interfacial boundaries.

3.2 Growth kinetics and mechanism of ABOw

3.2.1 *Influence of calcination temperature on growth process*

The growth of ABOw governs the microstructure of the aerogel, being directly influenced by the calcination temperature, the Al/B ratio in the raw materials, and the type of aluminum source used. Figures 4 and 5 show the SEM images of the ABOw grown within the matrix and on the mullite fibers, respectively, with different calcination temperatures and different Al/B ratios. Examination of the samples of different calcination temperatures with SEM revealed that the lowest temperature at which whiskers formed was 700 °C. Above this temperature, both the length and diameter of the whiskers progressively increased with rising temperature, and this holds true for samples with different Al/B ratios, as well as for whiskers growing on both the matrix and mullite fiber surfaces. The size increase is primarily governed by the diffusion-controlled Ostwald ripening process. As temperatures rise, diffusion rates increase exponentially, causing atoms on the surfaces of smaller whiskers to dissolve/evaporate/detach more

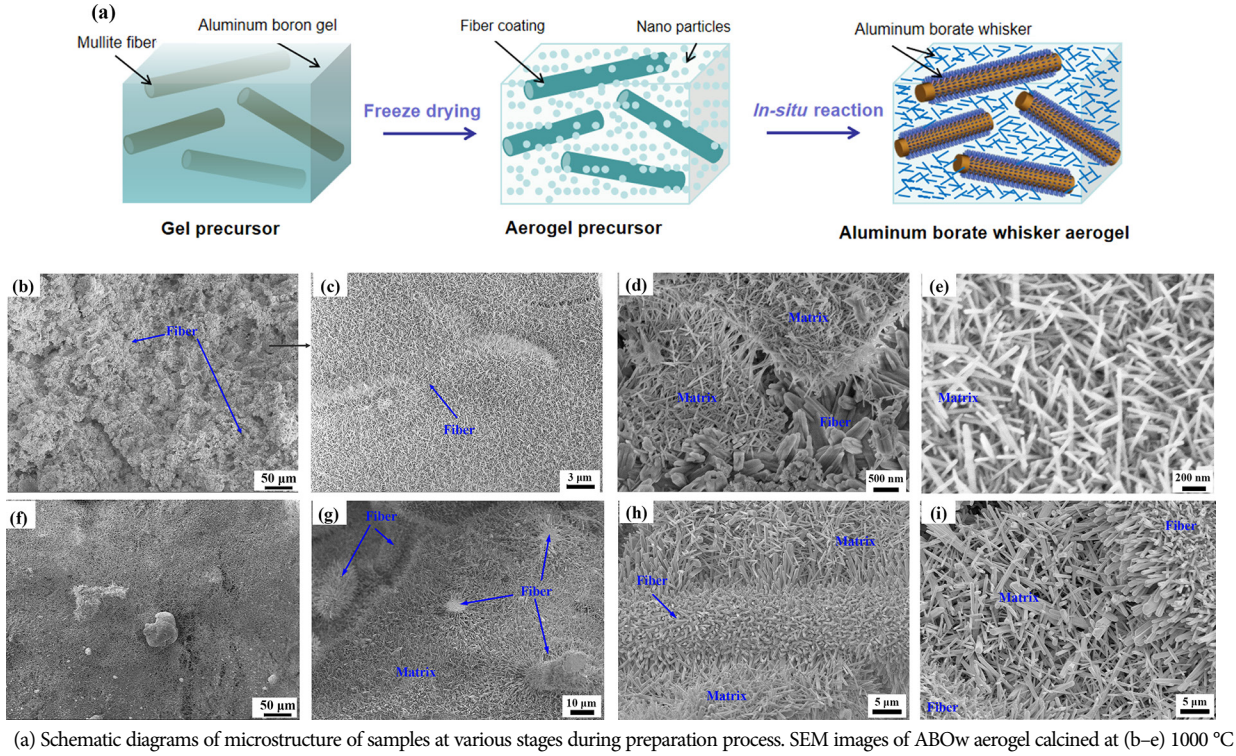

Fig. 3 (a) Schematic diagrams of microstructure of samples at various stages during preparation process. SEM images of ABOw aerogel calcined at (b–e) 1000 °C and (f–i) 1400 °C.

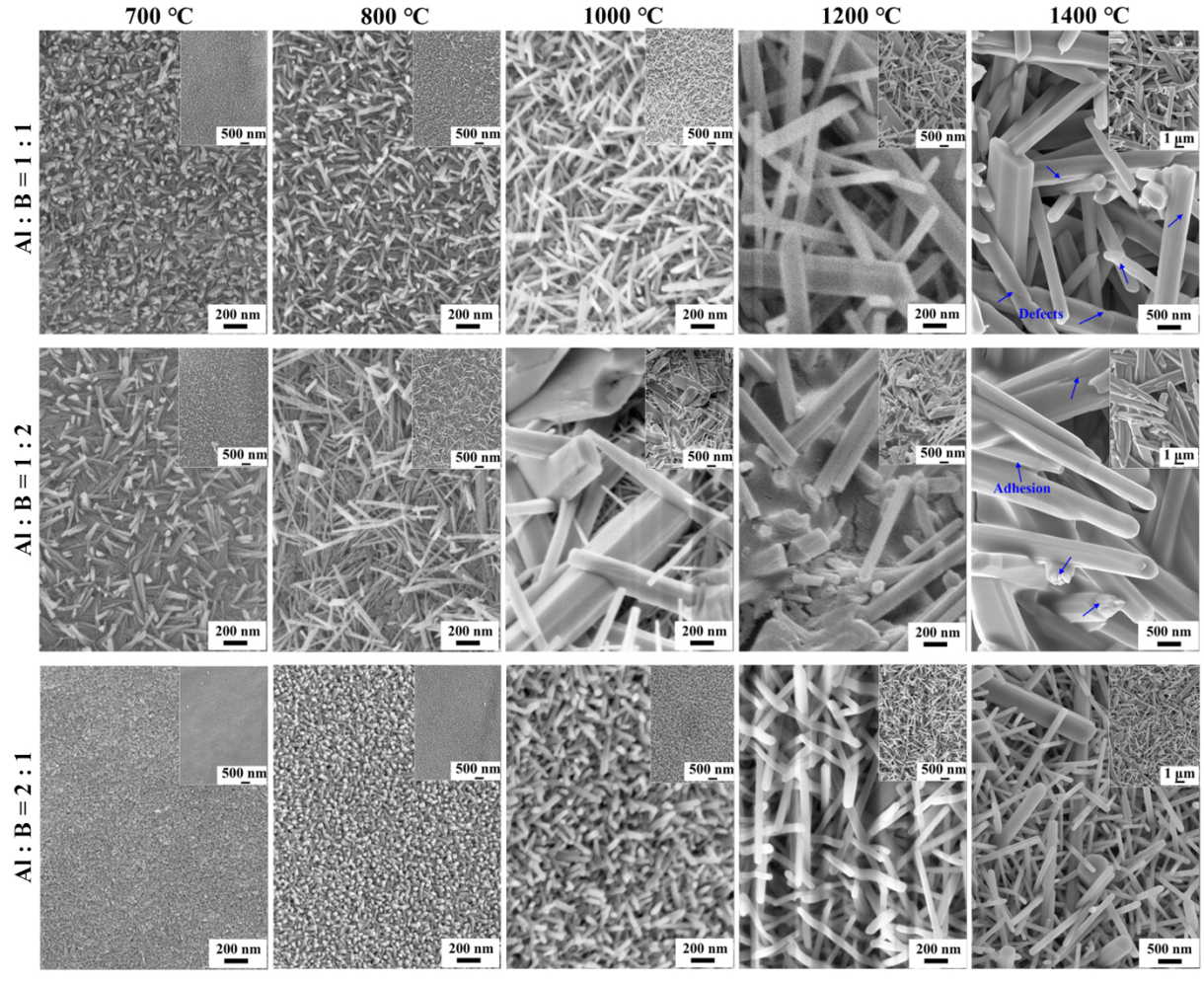

Fig. 4 SEM images of whiskers grown within matrix of ABOw aerogel with different calcination temperatures (700–1400 °C) and different Al/B ratios (1 : 1, 1 : 2, and 2 : 1).

readily. These atoms then migrate via vapor-phase or/and liquid-phase diffusion to deposit onto the surfaces of larger whiskers, resulting in rapid coarsening of larger whiskers, while smaller ones gradually diminish.

The calcination temperature also influences the crystal phase of ABOw. Figure 6(a) displays the XRD patterns of the samples with an Al/B ratio of 1 : 1 calcined at different temperatures. For 700 °C, only diffraction peaks corresponding to the raw materials (mullite and boric acid) are observed. This differs from the SEM observations (Fig. 4) showing whisker formation at 700 °C, which can be attributed to the extremely small dimensions of whiskers or their insufficient crystallinity. $Al_4B_2O_9$ begins to form at 800 °C, with diffraction intensity strengthening as the temperature increases. The high-temperature phase of aluminum borate ($Al_{18}B_4O_{33}$) emerges at 1100 °C. Above 1200 °C, the whiskers exclusively exist in the $Al_{18}B_4O_{33}$ phase, and the phase transition temperature varies among different samples and is influenced by the Al/B ratio.

To further characterize the formation and phase transition of ABOw, TEM was employed to examine samples with an Al/B ratio of 1 : 1 heat-treated at different temperatures, as shown in Fig. 7. After treatment at 700 °C, although no diffraction peaks of aluminum borate appeared in the XRD pattern, the TEM images (Figs. 7(a)–7(d)) clearly revealed a large number of monocrystalline whiskers with a diameter of approximately 10 nm and an aspect ratio greater than 10. The hemispherical tips of the whiskers indicate that their growth mechanism conforms to the V–L–S mechanism. The SAED pattern displays a series of concentric diffraction rings, which are the result of diffraction from numerous fine whiskers and were indexed to the $Al_4B_2O_9$ crystal. After being treated at 900 °C, the diameter and aspect ratio of the whiskers increased (Figs. 7(f)–7(i)), and SAED and high-magnification images identified it as $Al_4B_2O_9$. $Al_4B_2O_9$ belongs to the orthorhombic crystal system. Its fundamental building blocks are chains composed of [AlO_6] octahedra, which are interconnected via [AlO_4] tetrahedra and boron–oxygen polyhedra. The mixed coordination of boron includes both [BO_3] triangles and [BO_4] tetrahedra, as shown in Fig. 7(e). The lattice structure of the $Al_4B_2O_9$ whisker in Fig. 7(i) is schematically shown in Fig. 7(j), suggesting that [001] was the growth direction of individual $Al_4B_2O_9$ whiskers [30]. After being treated at 1200 °C, the whiskers exhibited a significant increase in crystal size (Figs. 7(k)–7(n)). The SAED results confirmed the formation of $Al_{18}B_4O_{33}$, while the straight whisker tips suggest a V–S growth mechanism. High-magnification images revealed a reduction in the interplanar spacing of the (220) planes, with the crystal growth direction remaining along the [001] direction. $Al_{18}B_4O_{33}$ belongs to the orthorhombic crystal system (Fig. 7(e)), and its main structure consists of [AlO_6] octahedra connected through corner sharing or edge sharing, forming double chains along the *c*-axis direction. These chains are further interconnected by [AlO_4] tetrahedra and [BO_3] triangles to form a three-dimensional network. This regular connectivity creates one-dimensional channels parallel to the *c*-axis within the crystal, which is the fundamental reason for its tendency to grow into rod-like or whisker morphologies [31]. Therefore, $Al_4B_2O_9$ is a relatively

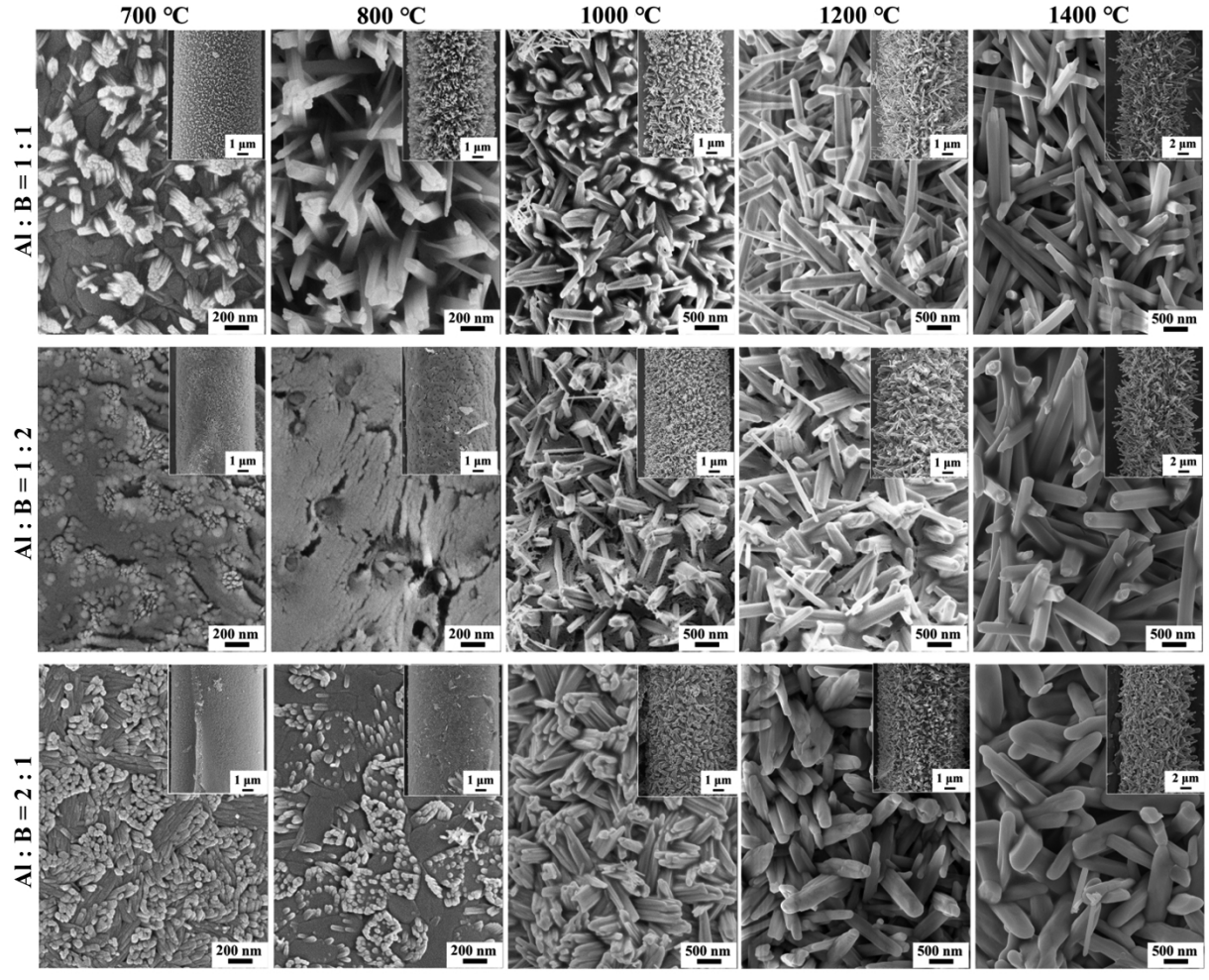

Fig. 5 SEM images of whiskers grown on mullite fiber surface in ABOw aerogel with different calcination temperatures (700–1400 °C) and different Al/B ratios (1 : 1, 1 : 2, and 2 : 1).

disordered, metastable intermediate-phase aluminum borate crystal, which transforms into a more stable crystal $Al_{18}B_4O_{33}$, at elevated temperatures (> 1100 °C).

Some studies describe the transformation of $Al_4B_2O_9$ to $Al_{18}B_4O_{33}$ with the chemical reaction $9Al_4B_2O_9 = 2Al_{18}B_4O_{33} + 5B_2O_3$ [18,20], while others, based on the phase diagram, express it as $Al_4B_2O_9 = Al_{18}B_4O_{33}$ + liquid [32,33]. From the Al_2O_3–B_2O_3 binary phase diagram as shown in Fig. S4 in the ESM, it is known that $Al_4B_2O_9$ is an incongruently melting compound in the system. It decomposes into $Al_{18}B_4O_{33}$ and a liquid phase rich in boron oxide at approximately 1100 °C.

3.2.2 *Influence of aluminum source on growth process*

In this experiment, the growth of ABOw within the matrix primarily utilized aluminum sol (Sol-A) as the aluminum source, whereas the whiskers on the fiber surface derived their aluminum source both from the aluminum sol and from the Al_2O_3 present in mullite. The difference in aluminum sources leads to distinct morphological characteristics between the whiskers within the matrix and those on the fiber surface. Quantitative image analysis based on SEM images in Figs. 4 and 5 reveals the diameters of ABOw in samples subjected to different calcination temperatures and with different Al/B ratios, as shown in Figs. 6(f)–6(h). During the process, measurements and statistical analysis of whisker diameters were performed using Nano Measure software. Multiple fields of view were selected for each sample, with no fewer than 200 whiskers measured per sample. Histograms of 18 samples showing the statistical distribution of measurements are presented in Fig. S5 in the ESM. As shown in Figs. 4 and 5, a large number of fine whiskers form within the matrix at lower temperatures (700–800 °C), interconnecting to create a porous structure, while the whiskers on the fiber surface remain embedded within a coating layer on the fiber surface. In all the samples calcined at temperatures of 700–1200 °C, the diameter of the whiskers within the matrix is significantly smaller than that of the whiskers on the fiber surface, regardless of the Al/B ratio. After treatment at 1400 °C, the diameter comparison of whiskers within the matrix and those on the fiber surface is influenced by the Al/B ratio. In addition, the aspect ratio and dimensions of the whiskers within the matrix exhibit a strong correlation with the Al/B ratio, whereas this relationship appears less pronounced for the whiskers on the fiber surface. In addition, there is also a significant difference in the growth kinetics of whiskers within the matrix and those on the fiber surface: The whiskers within the matrix gradually increase in diameter and aspect ratio between 700 and 1400 °C, with the diameter growing from approximately 10 nm to approximately 400 nm; in contrast, the whiskers on the fiber surface grow in clusters, and their diameter changes slowly with increasing temperature, remaining within the range of 200–400 nm. These differences arise from different whisker growth mechanisms and will be addressed in Section 3.2.4.

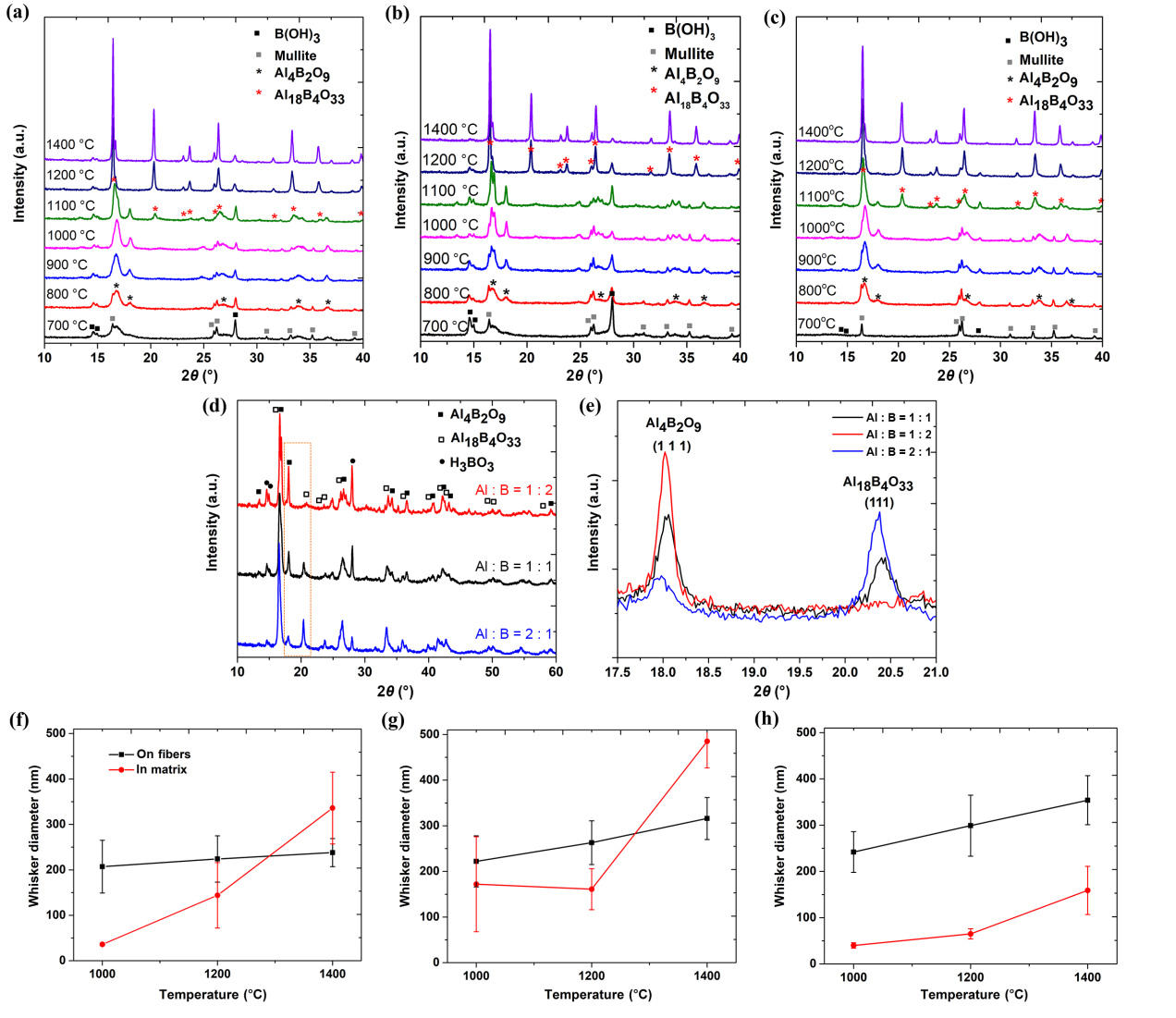

Fig. 6 XRD patterns of ABOw aerogel with different calcination temperatures, and Al/B ratios are (a) 1 : 1, (b) 1 : 2, and (c) 2:1. XRD patterns of (d) samples calcined at 1100 °C and (e) local magnification view within the 2 theta range of 17.5°–21.0°. Diameters of ABOw vary with calcination temperature for different Al/B ratios of (f) 1 : 1, (g) 1 : 2, and (h) 2 : 1.

3.2.3 *Influence of Al/B ratio on growth process*

The controlled Al/B ratios in this study specifically refer to the ratio between aluminum from aluminum sol (Sol-A) and boron from boron oxide. Thus, this parameter predominantly exerts a significant influence on the whisker growth within the matrix, as shown in Fig. 4. Within the calcination temperature range of 700–1400 °C, the whiskers formed within the matrix consistently exhibited a decrease in grain size with increasing Al/B ratio. This relationship manifested primarily as differences in the whisker aspect ratio at 700–800 °C, while at 1000–1400 °C, it was mainly reflected in variations in whisker diameter. The influence of the Al/B ratio on whisker dimensions can be explained as follows: When growing ABOw within the matrix at high temperatures, alumina governs nucleation, while boron oxide governs mass transfer [34]. B_2O_3 melts at approximately 500 °C and coats the surface of Al_2O_3 particles, where interfacial reactions occur between 600 and 700 °C, forming $Al_4B_2O_9$ crystal nuclei. The initial crystal growth primarily depends on the density of these nuclei, and excessively high nucleation density leads to competition among whiskers for limited gaseous reactants during the early growth stage, restricting the ultimate length of individual whiskers. Taking the matrix as an example (Fig. 4), a comparison was made of the nucleation density and grain size of samples with different Al/B ratios after calcination at 700 °C. After treatment at 700 °C, all samples formed a large number of fine aluminum borate crystals. At an Al/B ratio of 1 : 1, well-defined slender rod-shaped crystals were observed, with individual crystal lengths of approximately 150–250 nm and diameters of 30–50 nm. These crystals exhibited a high aspect ratio and a moderate number of crystals. At an Al/B ratio of 1 : 2, the crystals were also rod-shaped but appeared thicker and sturdier, with lengths reaching 300–450 nm and diameters of 50–80 nm. The number of crystals was noticeably lower. At an Al/B ratio of 2 : 1, the morphology changed to quasi-spherical nanoparticles with diameters of approximately 20–50 nm, showing no distinct anisotropy. In this case, the number of nuclei was clearly the highest. Therefore, samples with a higher Al/B ratio exhibit higher nucleus density and shorter lengths. The growth rate of the whiskers is mainly determined by the rate and concentration of active gaseous/liquid reactants transported to the growth interface. At high temperatures, boron oxide both melts and volatilizes, giving it a mass transfer capability far greater than that of alumina. Consequently, whiskers in boron-rich samples exhibit faster axial growth rates and achieve greater lengths.

The Al/B ratio also affects the phase transition temperature of ABOw. The XRD patterns at different temperatures for the samples with various Al/B ratios are shown in Figs. 6(a)–6(c). The initial diffraction peaks of $Al_4B_2O_9$ appear at 800 °C for all the samples. As the temperature increases, samples with Al/B ratios of 1 : 1 and 2 : 1 begin to form $Al_{18}B_4O_{33}$ at 1100 °C, exhibiting the coexistence of $Al_4B_2O_9$ and $Al_{18}B_4O_{33}$. When the temperature rises to 1200 °C and above, the phase transforms into $Al_{18}B_4O_{33}$. In contrast, for the sample with an Al/B ratio of 1 : 2, the diffraction peaks of $Al_{18}B_4O_{33}$ do not appear until 1200 °C. A comparison of the XRD patterns of the samples treated at 1100 °C (Figs. 6(d) and 6(e)) more clearly reveals this difference: The relative content of $Al_4B_2O_9$ to $Al_{18}B_4O_{33}$ decreases as the Al/B ratio increases. The reason is as follows: Above 1100 °C, the noticeable volatilization of B_2O_3 facilitates the transition from the boron-rich phase $Al_4B_2O_9$ (Al/B = 2 : 1) to the aluminum-rich phase $Al_{18}B_4O_{33}$ (Al/B = 9 : 2). Under high-temperature phase equilibrium, their relative content is thermodynamically governed by the initial Al/B stoichiometric ratio. When the B_2O_3 content in the system increases, the limited availability of Al_2O_3 becomes a restricting factor, allowing the $Al_4B_2O_9$ phase, which accommodates more B_2O_3, to remain relatively stable. This results in an increase in its relative content as the B_2O_3 content rises.

3.2.4 *Growth mechanisms of ABOw*

The above findings demonstrate that during the growth of ABOw on the mullite fiber surfaces and within the matrix, the whisker morphology is significantly influenced by both the calcination temperature and the B/Al ratio, with distinctly different patterns of dependence. This suggests corresponding variations in the underlying growth mechanisms. Therefore, we conducted further characterization of the aerogels with an Al/B ratio of 1 : 1 subjected to different calcination temperatures (Figs. 8(a)–8(l)) and separately determined the growth mechanisms of ABOw within the matrix and on the mullite fiber surface (Fig. 8(m)).

The growth process of ABOw within the matrix is discussed first (Fig. 8(m)). After drying, the matrix is filled with nanoparticles containing the aluminum borate precursor formed by the dehydration and condensation of the aluminum–boron sol (Fig. 8(a)). As the temperature increases, the hydrates decompose, and bound water volatilizes. When the temperature exceeds 450 °C, B_2O_3 begins to melt, coating the surface of the Al_2O_3 nanoparticles. With further temperature elevation, B_2O_3 and Al_2O_3 react at the interface to form aluminum borate nuclei ($B_2O_3 + Al_2O_3 = Al_4B_2O_9$). The presence of molten B_2O_3 and the confined sintering environment facilitate vapor and liquid phase mass transfer, enabling crystals to grow along their [001] direction into fine needle-like crystals, following the V–L–S mechanism. Although different from most V–L–S growth processes involving metal catalysts, this system is considered to exhibit a self-catalytic mechanism [20,35,36]. Starting at 450 °C, a B_2O_3 melt begins to form. At higher temperatures, according to the B_2O_3–Al_2O_3–SiO_2 ternary phase diagram [32], borosilicate liquid phases and aluminoborosilicate liquid phases gradually develop, enabling liquid-phase mass transfer. In some boron-rich samples, spherical features have been observed (Fig. S6 in the ESM). EDS elemental mapping analysis indicates that these features contain silicon and oxygen but no aluminum. Boron cannot be detected by EDS, and it is speculated that it likely constitutes a borosilicate phase formed during the solidification of a melt. Furthermore, experimental observations show that samples calcined in non-enclosed environments exhibit poor whisker growth, indicating that vapor-phase mass transfer is also essential. SEM observations (Figs. 8(b) and 8(c)) reveal that only nanoparticles exist within the matrix after 600 °C treatment, while needle-like crystals are uniformly generated within the matrix after 700 °C treatment, suggesting that the initial formation temperature of aluminum borate crystal nuclei is between 600 and 700 °C. As the calcination temperature further increases, the Ostwald ripening process continues, gradually increasing the crystal diameter and aspect ratio of the

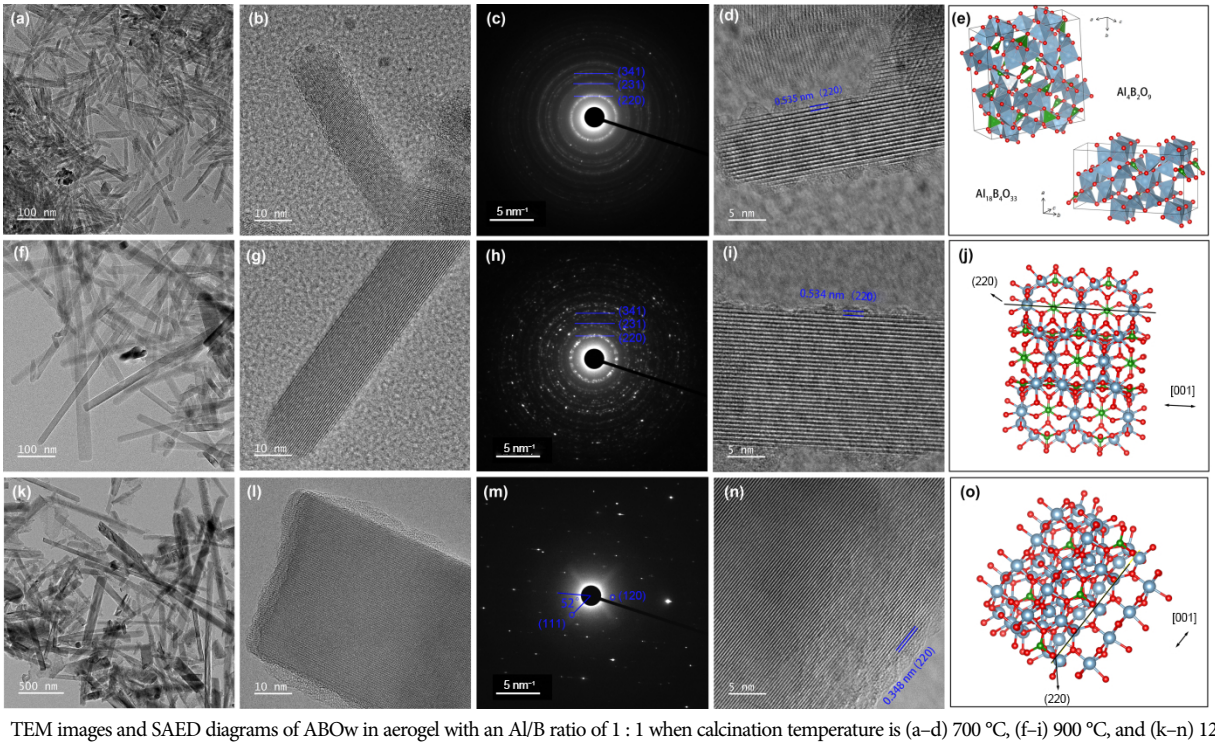

Fig. 7 TEM images and SAED diagrams of ABOw in aerogel with an Al/B ratio of 1 : 1 when calcination temperature is (a–d) 700 °C, (f–i) 900 °C, and (k–n) 1200 °C. Lattice structure schematic diagrams of (e) $Al_4B_2O_9$ and $Al_{18}B_4O_{33}$, (j) structure in (i), and (o) structure in (n).

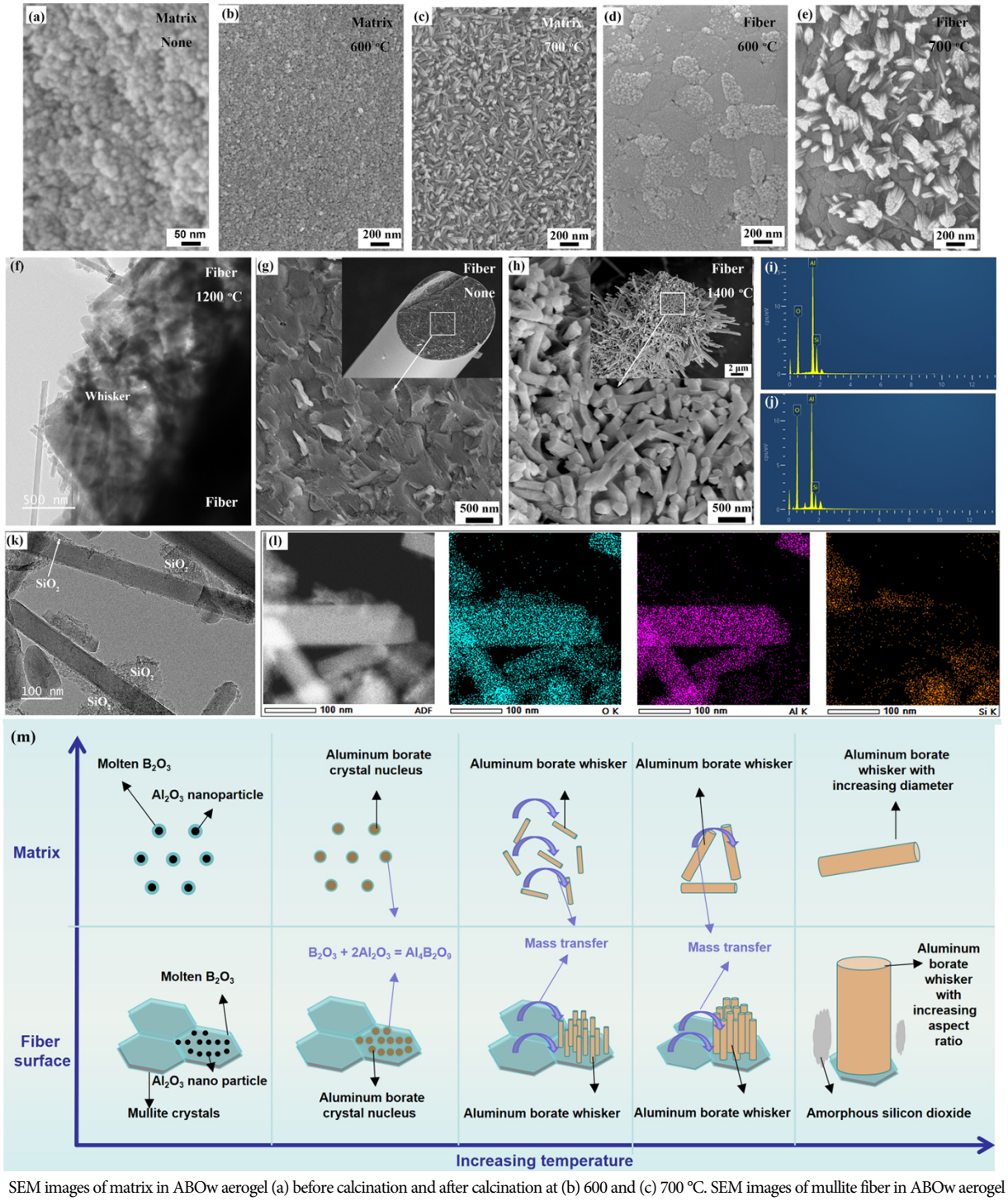

Fig. 8 SEM images of matrix in ABOw aerogel (a) before calcination and after calcination at (b) 600 and (c) 700 °C. SEM images of mullite fiber in ABOw aerogel when calcination temperature is (d) 600 °C, (e) 700 °C, (g) raw, and (h) 1400 °C. EDS analyses of (i) area within box in (g, j) in (h). (f, k) TEM images of mullite fiber in aerogel when calcination temperature is 1200 °C and (l) localized EDS mapping. (m) Schematic diagram of growth mechanism of ABOw within matrix and on mullite fiber surface.

ABOw, as shown in Fig. 4. The growth and phase transformation of whiskers during the subsequent temperature rise process have been discussed in Section 3.2.1.

In contrast, the whisker growth process on the surface of mullite fibers is different. After B_2O_3 starts to melt, it will cover the surface of the mullite fibers. After treatment at 600 °C (Fig. 8(d)), distinct grain boundaries can be observed on the surface of the polycrystalline mullite fibers, with grain sizes measuring approximately 200–300 nm. The surfaces of some grains are covered with a layer of nanoparticles, which are speculated to be aluminum borate nuclei. Mullite belongs to the orthorhombic crystal system. Along the *c*-axis ([001] direction), [AlO_6] octahedra are connected through edge-sharing or corner-sharing, forming continuous parallel chains, which are interconnected via [SiO_4] tetrahedra and some [AlO_4] tetrahedra. Its analogous crystal structure to aluminum borate may enable certain oriented mullite grains to act as substrates for aluminum borate crystal growth, thereby promoting the aggregation of aluminum borate nuclei on their exposed low-surface-energy crystal planes. When the temperature is raised to 700 °C (Fig. 8(e)), the nuclei grow into

whiskers. ABOw grows in clusters on the surface of individual mullite grains, while no whisker growth is observed on the surfaces of other differently oriented mullite grains. As the temperature further increases, the fine, clustered ABOw gradually coalesces into a single thick whisker, as shown in Fig. 5. This consolidated whisker continues to elongate with rising temperature, with its diameter approaching the original grain size of the mullite. TEM observation (Figs. 8(f) and 8(k)) of the whiskers on the fiber surface after 1200 °C treatment reveals the presence of amorphous, irregularly shaped material between the whiskers. EDS mapping (Fig. 8(l)) analysis shows that this material is enriched with silicon and oxygen, suggesting that it is silica. This indicates the decomposition of mullite fibers into SiO_2 and Al_2O_3, suggesting that the precipitated Al_2O_3 participates as an aluminum source in the growth of the ABOw. Cross-sectional observation of the fibers after treatment at 1400 °C (Fig. 8(h)) reveals that the ABOw extends deep into the fiber interior, forming an interwoven whisker network. EDS analysis (Figs. 8(i) and 8(j)) demonstrates a decrease in silicon content and an increase in oxygen content within the fibers compared with the original mullite fibers, which further corroborates the hypothesis that Al_2O_3 from the mullite fibers serves as the aluminum source to grow ABOw. Therefore, the presence of B_2O_3 lowers the decomposition temperature of mullite, creating a ternary region composed of Al_2O_3, B_2O_3, and SiO_2 in the vicinity of the fibers. The eutectic phase formed by SiO_2 and B_2O_3 facilitates liquid-phase mass transport and promotes the growth of ABOw. The significant decrease in the decomposition temperature of the mullite is mainly due to two factors. First, polycrystalline mullite fibers prepared by the melt-blown method have finer grains (tens of nanometers to submicrons) and higher contents of free silica and alumina than conventional mullite ceramics, resulting in inferior temperature resistance [20]. In addition, according to the Al_2O_3–SiO_2–B_2O_2 ternary phase diagram [32], although mullite itself is stable below 1400 °C, the temperature for liquid phase formation is significantly reduced in the presence of abundant boron oxide, and the liquidus temperature decreases further with higher boron content. Therefore, B_2O_3 forms a eutectic mixture with free silica at lower temperatures (1000–1400 °C), accelerating the decomposition of mullite. Mullite decomposition to form $Al_{18}B_4O_{33}$ at 1100 °C in Al_2O_3–SiO_2–B_2O_3 fibers has also been documented in Ref. [37].

3.3 Properties of ABOw aerogel

FTIR spectroscopy was employed to characterize the variations in chemical bonds of the ABOw aerogel samples at different stages of the synthesis process, as shown in Fig. 9(a). The peak at a wavenumber of 3215 cm^{-1} is attributed to water group vibrations. The wide band with a maximum peak next to 1457 cm^{-1} and the peak at 1186 cm^{-1} are assigned to the asymmetric and symmetric stretching vibrational modes of the B–O bond, respectively. The peak at approximately 710 cm^{-1} represents the flexible vibrations of the B–O–B associates of most borates [38,39]. The peak at approximately 1072 cm^{-1} is associated with Al–O stretching vibrations. The presence of both Al–O vibrations and the previously mentioned B–O vibrations in the dried precursor collectively indicates the formation of a B–O–Al network. Following high-temperature calcination, the broad absorption band sharpened significantly and exhibited well-resolved splitting. This indicates a more uniform vibrational environment, enhanced structural ordering, and increased harmonicity of the lattice vibrations after the precursor crystallized into ABOw. The bands between 1200 and 1500 cm^{-1} are due to the non-bridging and symmetric stretching vibrations of B–O in triangular $[BO_3]$ units, and the bands between 800 and 1200 cm^{-1} are due to the stretching vibrations of B–O bonds in $[BO_4]$ [40,41]. The presence of four bands at approximately 1261, 1341, 1396, and 1423 cm^{-1} suggests the presence of four different environments for B–O in $[BO_3]$. In addition, the bands between 814 and 640 cm^{-1} are attributed to the bending vibrations of O–B–O in $[BO_3]$ and $[BO_4]$. The bands between 750 and 950 cm^{-1} and between 500 and 650 cm^{-1} are attributed to the stretching vibrations of Al–O in tetrahedral $[AlO_4]$ and octahedral $[AlO_6]$ units, respectively [42]. In contrast to the sample calcined at 1000 °C, the sample treated at

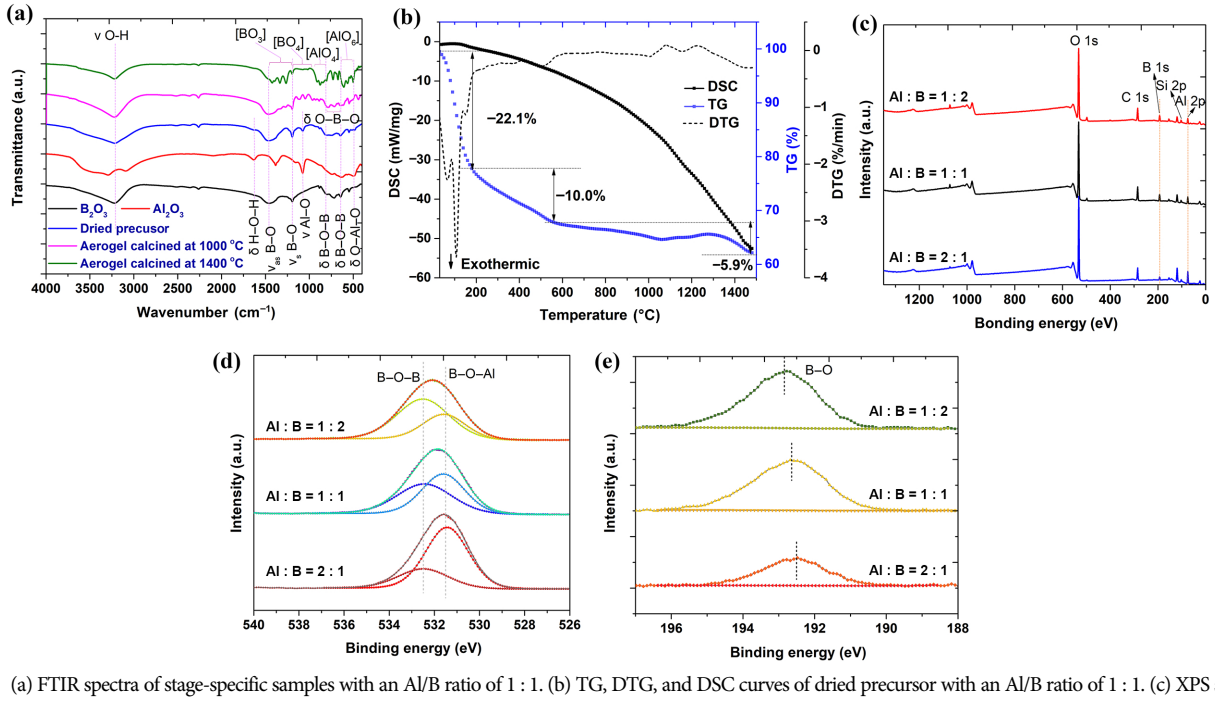

Fig. 9 (a) FTIR spectra of stage-specific samples with an Al/B ratio of 1 : 1. (b) TG, DTG, and DSC curves of dried precursor with an Al/B ratio of 1 : 1. (c) XPS survey spectra, (d) O 1s and (e) B 1s fine spectra of aerogels calcined at 1400 °C.

清華大学出版社 Tsinghua University Press | SciOpen

1400 °C shows the disappearance of the [BO_4] peak and an intensification of the [BO_3] absorption band, demonstrating that the products obtained at 1000 and 1400 °C are $Al_4B_2O_9$ and $Al_{18}B_4O_{33}$, respectively.

The TG, differential TG (DTG), and DSC curves of the dried precursor with an Al/B ratio of 1 : 1 are shown in Fig. 9(b). For the TG curve, a rapid mass loss of approximately 22.1%, occurring primarily before 180 °C, is attributed to the evaporation of free water. This is likely due to moisture absorption from the air by the freeze-dried precursor. The mass loss between 180 and 560 °C corresponds mainly to the removal of bound water, such as crystalline water, structural hydroxyl groups, and water generated from the decomposition of boric acid. Beyond 560 °C, the mass loss rate decreases until it increases again after 1300 °C. This final stage involves the continuous and slow volatilization of B_2O_3, which accelerates significantly at elevated temperatures. Due to the high heating rate (10 °C/min), the actual volatilization of B_2O_3 is less than expected; however, the extent of volatilization during the actual synthesis process, which involves prolonged high-temperature holding (2 h), remains unknown. The DSC curve exhibits a broad exothermic profile without sharp peaks. This is primarily because the underlying diffusion-controlled solid–liquid/solid-state processes, including dissolution, diffusion, reaction, and crystallization, continuously occur over a wide temperature range. Furthermore, the endothermic effect of melting and subsequent volatilization of B_2O_3 overlaps with the exothermic reaction of synthesizing ABOw in the high-temperature region, which attenuates the net exothermic signal on the DSC curve, making it difficult to form sharp peaks.

To further investigate the volatilization and chemical states of B_2O_3 in samples with different Al/B ratios after calcination, XPS analysis was performed on the samples calcined at 1400 °C, as shown in Fig. 9(c). All samples contain five elements: Al, Si, O, B, and C. The Al/B ratio significantly deviates from that in the starting materials, which is attributed to three main factors: the introduction of additional aluminum from the mullite fibers, partial volatilization of B_2O_3, and inherent compositional heterogeneity between the surface and the bulk of the samples. The high-resolution O 1s spectra (Fig. 9(d)) exhibits two primary peaks. The peak at a binding energy of 532.48 eV is assigned to B–O–B bonds, primarily originating from residual B_2O_3. The peak at 531.48 eV is assigned to B–O–Al bonds, primarily from the formed aluminum borate [43]. This latter peak can be further deconvoluted, potentially revealing a contribution from Al–O–Al bonds at an even lower binding energy. The proportion of B–O–B increases with the initial B_2O_3 content in the precursor, indicating a greater amount of unreacted B_2O_3 residue. This finding is consistent with the results obtained from XRD analysis (Figs. 6(a)–6(c)). The B 1s peak (Fig. 9(e)), located in the binding energy range of 192.5–192.9 eV, corresponds to three-coordinated boron with sp^2 hybridization [44–46]. This is consistent with the boron coordination in B_2O_3, boric acid, and $Al_{18}B_4O_{33}$, aligning with our previous analysis. In the $B(OH)_3$ unit of boric acid, the hydrogen atoms on the oxygen withdraw electron density via an inductive effect, leading to a slightly higher binding energy for the central B. Therefore, the binding energy of the B–O bond peak exhibits a positive shift with increasing initial B_2O_3 content in the precursor, attributed to a greater proportion of boron existing in the form of boric acid.

3.4 Performance of ABOw aerogel

3.4.1 Basic physical properties

The densities of the samples calcined at different temperatures are presented in Fig. 10(a). The uncalcined samples exhibited the highest density, approximately 0.288–0.296 g/cm^3. For all Al/B ratios, the density showed a decreasing trend with increasing calcination temperature, primarily attributed to the removal of water and the volatilization of B_2O_3. A noticeable difference in density was observed among samples with different Al/B ratios. Samples with a higher initial boron content experienced a more significant density reduction as the calcination temperature increased. Consequently, the samples with an Al/B ratio of 2 : 1 consistently demonstrated the highest density (0.231–0.243 g/cm^3), followed by those with a 1 : 1 ratio (0.206–0.227 g/cm^3), and the samples with a 1 : 2 ratio had the lowest density (0.173–0.210 g/cm^3). The disparity in density among these three groups became more pronounced at higher temperatures.

The specific surface area (SSA) of the ABOw aerogel with different Al/B ratios and calcination temperatures is shown in Fig. 10(b). The SSA decreased significantly with increasing calcination temperature, a trend particularly pronounced for the sample with an Al/B ratio of 2 : 1. For this composition, the SSA dropped from 34.0 m^2/g at 1000 °C to 3.5 m^2/g at 1400 °C, which can be attributed to the crystal growth of ABOw at elevated temperatures. In contrast, the samples with Al/B ratios of 1 : 1 and 1 : 2 consistently exhibited low SSAs (< 5 m^2/g) after calcination at 1000–1400 °C. The nitrogen adsorption–desorption experiments (Figs. 10(c)–10(h)) also demonstrated that the adsorption capacity decreases with increasing calcination temperature of the samples and increases with a higher Al/B ratio in the samples. This is because the Al/B ratio affects the size of ABOw within the matrix. As shown in Fig. 4, after various heat treatments (700–1400 °C), the sample with an Al/B ratio of 2 : 1 exhibits finer and denser whiskers, resulting in a larger surface area. It should be noted that although BET tests were not conducted on samples treated below 1000 °C, it can be inferred that lower calcination temperatures (700–900 °C) would result in a larger SSA and adsorption capacity due to their finer grains and smaller pore sizes.

The thermal conductivity of the ABOw aerogel with different Al : B ratios is shown in Fig. 10(i). The thermal conductivity of all samples ranges between 0.0560 and 0.0873 W/(m·K), indicating that the material is an excellent thermal insulator. As the calcination temperature increases from 1000 to 1400 °C, all samples exhibit a marked increasing trend in thermal conductivity, which is the result of the combined influence of multiple heat transfer mechanisms. At room temperature, thermal radiation is weak and can be neglected. According to the mixing rule, lower sample density and higher porosity result in fewer solid conduction paths, which typically lead to lower thermal conductivity. However, in this system, the variation trends of density and thermal conductivity with calcination temperature are opposite, indicating that this is evidently not the key influencing factor in this system. Therefore, the key influencing factors are the reduction in heat convection and the increase in interfacial thermal resistance caused by refined whiskers and pore sizes. In the aerogel assembled from a large number of ABOw, heat undergoes severe scattering at the interfaces between these nanounits, generating significant interfacial thermal resistance [47,48]. The lower the calcination temperature, the smaller the whisker size, resulting in more interfaces and greater thermal resistance. Moreover, a lower calcination temperature leads to a smaller average pore size. When the pore size approaches the mean free path of air molecules, gaseous conduction is significantly weakened due to the Knudsen effect, further reducing the thermal conductivity [42,49]. At calcination temperatures between 1000 and 1400 °C, samples with an Al/B ratio of 1 : 1

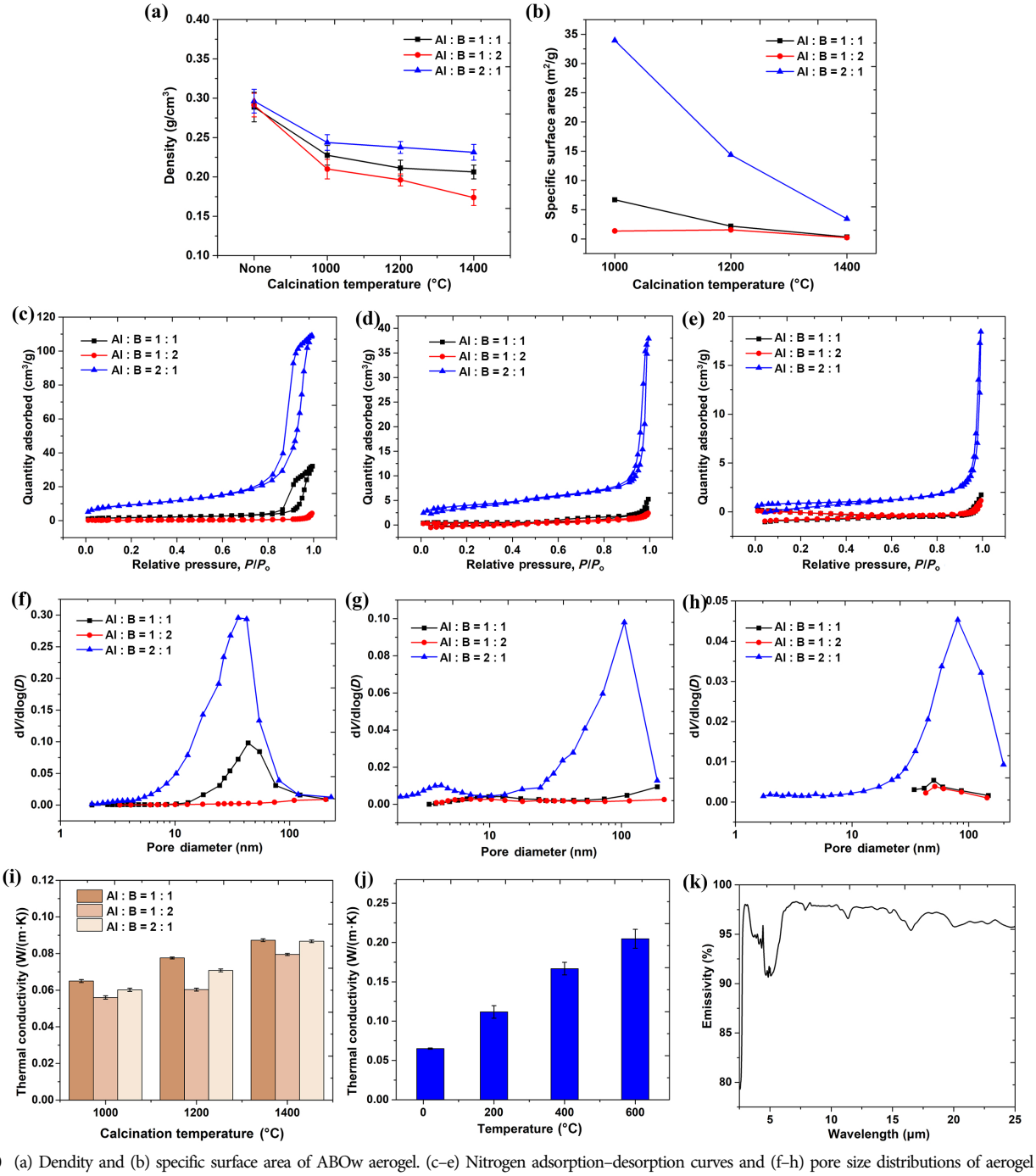

Fig. 10 (a) Dendity and (b) specific surface area of ABOw aerogel. (c–e) Nitrogen adsorption–desorption curves and (f–h) pore size distributions of aerogel with different Al/B ratios with calcination temperatures of (c, f) 1000 °C, (d, g) 1200 °C, and (e, h) 1400 °C. (i) Thermal conductivity of ABOw aerogel. (j) High-temperature thermal conductivity and (k) emissivity of aerogel with an Al/B ratio of 1 : 1 and calcined at 1000 °C.

consistently exhibit the highest thermal conductivity, those with a ratio of 2 : 1 show intermediate values, and samples with a ratio of 1 : 2 display the lowest thermal conductivity. The reduction in thermal conductivity in the latter two cases is primarily attributed to refined whisker/pore structures and lower density, respectively.

The high-temperature thermal conductivity of the ABOw aerogel with an Al/B ratio of 1 : 1 calcined at 1000 °C is shown in Fig. 10(j). The thermal conductivity increases significantly with increasing temperature, reaching 0.2047 W/(m·K) at 600 °C, which is caused by the increased contribution from gaseous thermal conduction and thermal radiation. Due to the small average pore size in ABOw aerogels, gaseous conduction is relatively limited, and the main influencing factor is thermal radiation. The spectral emissivity of the ABOw aerogel in the wavelength range of 2.5–25 μm is shown in Fig. 10(k). The spectral emissivity exceeds 0.95 in the wavelength range of 7–25 μm, while it is lower but still above 0.9 at shorter wavelengths. The spectral emissivity pattern is similar to that of most oxide ceramics, which exhibit high transmittance in the low-wavelength range and possess excellent emissivity in the high-wavelength range [50,51]. The hemispherical total emissivity is 0.97, and good infrared radiative performance contributes to reducing the thermal conductivity of the material at high temperatures. In summary, the ABOw aerogels exhibit relatively low thermal conductivity and meet the insulation requirements for high-temperature thermal protection materials.

3.4.2 *Mechanical properties*

The compressive stress–strain curves of the ABOw aerogel with an Al : B ratio of 1 : 1 calcined at different temperatures are shown in Fig. 11(a). The samples calcined at different temperatures exhibit similar curve profiles, with a significant strain tolerance benefiting from the mullite fiber (below 1200 °C) or the columnar reinforcement assembled from ABOw derived from mullite fibers at temperatures above 1200 °C. The initial linear elastic stage indicates that the material undergoes reversible elastic deformation under low stress, primarily dominated by the elastic bending and stretching of the skeletal units of aerogel. Compared with the plateau region (the second stage) observed in pure aerogel materials, the curves of the fiber-reinforced aerogels transition into a broad, gradually ascending peak because the fiber network bears the majority of the load, preventing large-scale collapse of the matrix and resulting in a more controllable failure process [52,53]. The multiple noticeable stress fluctuations observed in the curve may correspond to the fracture of fibers within the aerogel. Consequently, the material can absorb significantly more energy during compression through mechanisms such as fiber bridging, interfacial debonding, and fiber pull-out. The full-range compressive stress–strain curve of the sample with an Al/B ratio of 1 : 1 calcined at 1000 °C is shown in Fig. 11(b). The result shows that if the strain increases beyond a certain point (e.g., over 50%), most of the porous structure collapses, and the material enters the densification stage, characterized by a sharp increase in stress with further strain. Compression-rebound testing was conducted on the sample under a fixed strain of 10%, with the curve shown in the inset in Fig. 11(b). The aerogel exhibits an elastic recovery rate of less than 2%, indicating negligible elasticity. In other words, compared with particulate aerogels and fibrous aerogels, the mechanical behavior of the ABOw aerogel is closer to that of the former. This is primarily attributed to the inherent stiffness of aluminum borate whiskers, which lack the bendability of nanofibers, combined with their low aspect ratio that limits effective intertwining and physical entanglement between whiskers.

Since the stress continues to rise as the strain increases, the compressive strength of the ABOw aerogel was defined as the stress at 10% strain. The variations in the strength and Young's modulus with calcination temperature are shown in Figs. 11(c) and 11(d). Samples with different Al/B ratios all exhibit a consistent trend in strength: It initially increases and then decreases with increasing calcination temperature. For most aerogels, a higher density implies more solid material per unit volume and a sturdier skeleton, with strength generally being proportional to the square or a higher power of density. In this specific system, although the density decreases as the calcination temperature increases (Fig. 10(a)), the building blocks (ABOw) of the aerogel undergo significant structural changes during calcination, which dominate the variation in strength. Compared with samples treated at 1000 °C, those treated at 1200 °C show a marked increase in whisker diameter and aspect ratio (Fig. 4), greatly enhancing the load-bearing capacity of individual whiskers. In addition, the increased bridging area between whiskers strengthens the nodal connections [54,55]. In addition, the increase in the aspect ratio of the whiskers on the mullite fiber surface (Fig. 5) facilitates interfacial stress transfer with the whiskers within the matrix, thereby enhancing the overall strength. However, when the treatment temperature rises to 1400 °C, the strength declines, and this drop is more pronounced in samples with higher B_2O_3 content. SEM images (Fig. 4) reveal that while the whisker size increases further at 1400 °C compared with that at1200 °C, surface defects emerge. This is particularly evident in samples with an Al/B ratio of 1 : 2, where distinct whisker adhesion, surface melting, and deformation are observed. This indicates that excessive temperature leads to overgrowth of crystals and the formation of a eutectic phase due to the presence

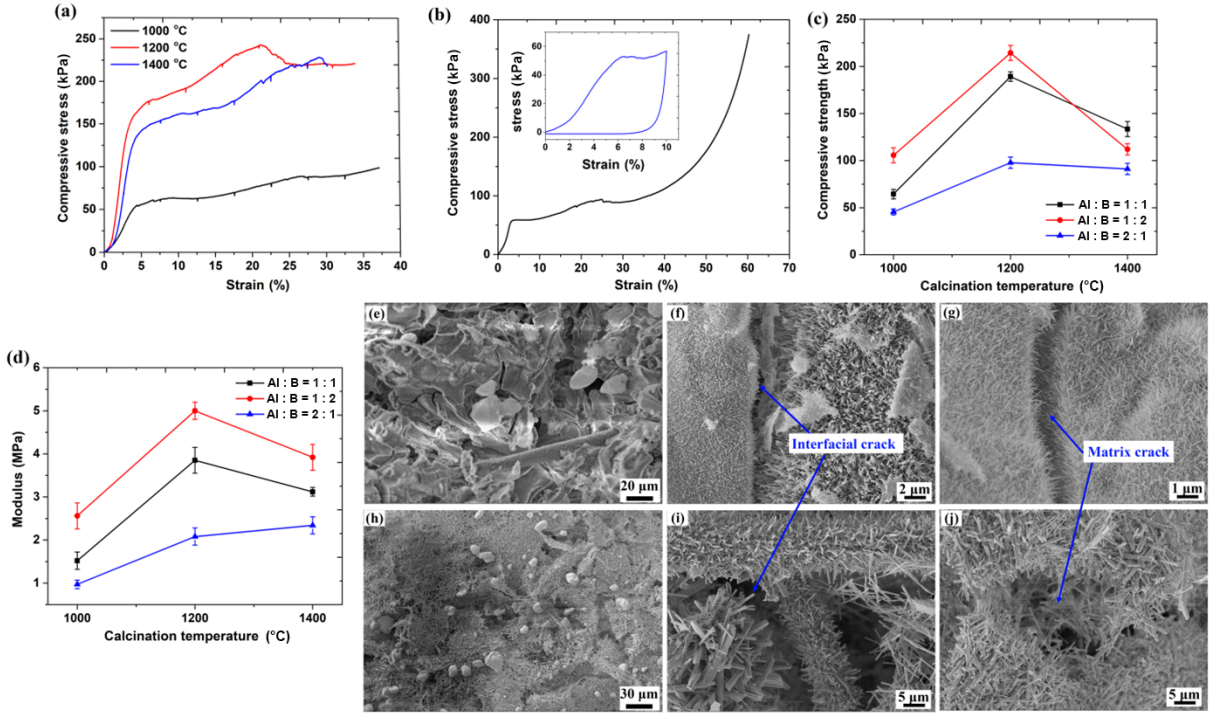

Fig. 11 (a) Compressive stress–strain curves of ABOw aerogel with an Al/B ratio of 1 : 1, (b) full-range curve and loading–unloading curve of sample with an Al/B ratio of 1 : 1 calcined at 1000 °C, and variation in (c) strength and (d) Young's modulus with calcination temperature. Microscopic morphology of samples with an Al/B ratio of 1 : 1 calcined at (e–g) 1000 °C and (h–j) 1400 °C after 20% compression.

of B_2O_3, which introduces defects into the skeleton, ultimately causing the strength reduction. Beyond the calcination temperature, the Al/B ratio critically determines the strength, with higher boron content consistently yielding stronger samples at both 1000 and 1200 °C. The strengthening mechanism operates by promoting larger whisker growth and simultaneously utilizing excess B_2O_3 as inter-whisker "welding points" that reinforce the junctions and enable effective stress transfer.

To illustrate the main failure modes of the ABOw aerogel after compression, morphological characterization was performed on the samples with an Al/B ratio of 1 : 1 calcined at 1000 and 1400 °C after 20% compression, and the SEM images are shown in Figs. 11(d)–11(f) and 11(g)–11(i), respectively. Following compressive failure, distinct matrix cracking and interfacial cracking between the fibers and the matrix are observed in the samples, while no obvious fiber pull-out or fiber fracture is observed.

3.4.3 *Temperature resistance*

To further investigate the high-temperature resistance of the ABOw aerogel and determine its high-temperature failure modes, we employed two treatment conditions: holding at 1400 °C for 20 h and holding at 1500 °C for 2 h to examine its high-temperature durability and temperature resistance limit, respectively. The test results are shown in Fig. 12.

After treatment at 1400 °C/20 h, the ABOw aerogels with

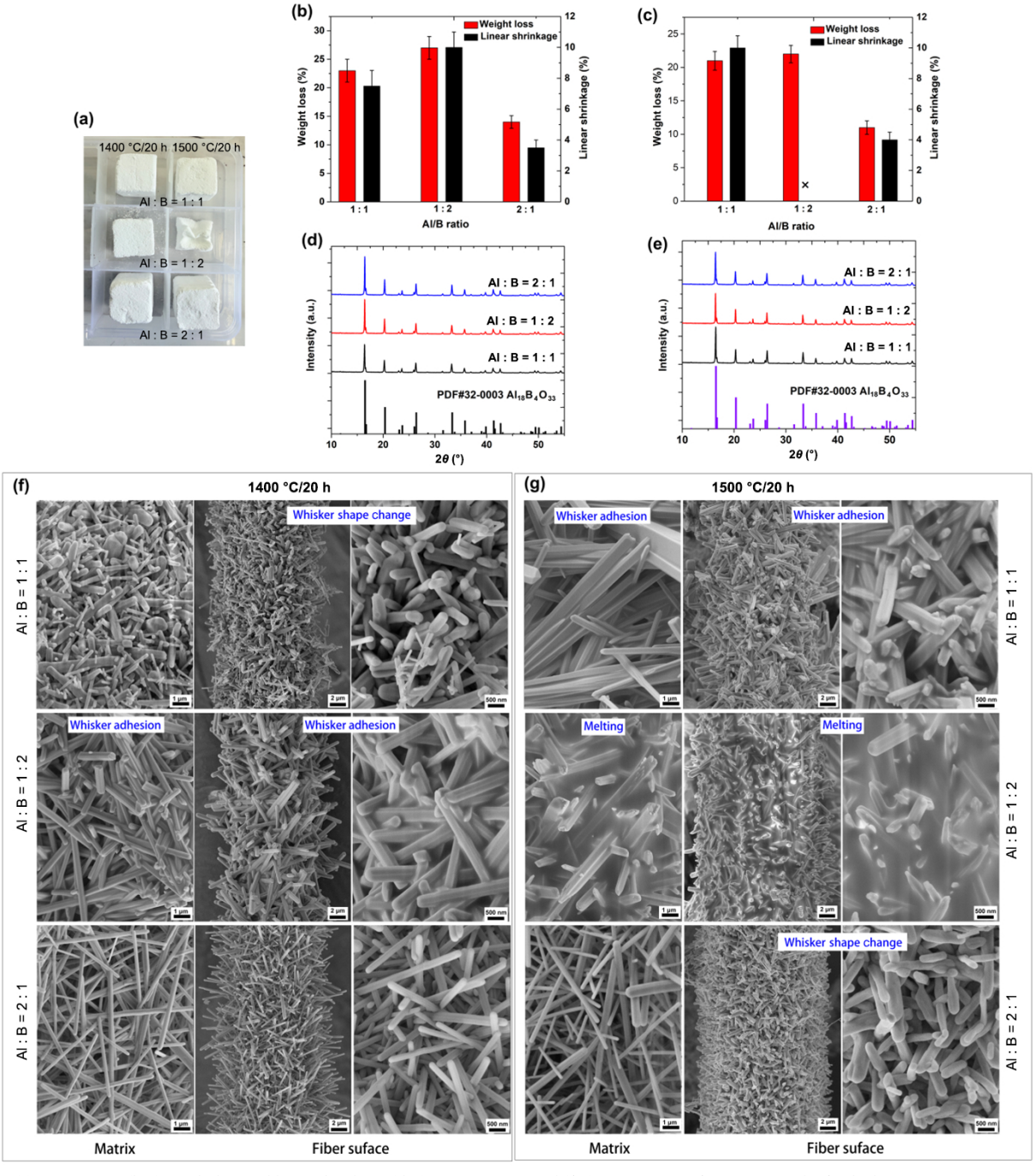

Fig. 12 (a) Appearance, (b, c) weight loss and linear shrinkage, (d, e) XRD patterns, and (f, g) SEM images of ABOw aerogels after high-temperature treatment. Heat treatment conditions are as follows: (b, d, f) held at 1400 °C for 20 h and (c, e, g) held at 1500 °C for 2 h.

Table 3 Comprehensive performance comparison of high-temperature resistant aerogels

Areogel	Density (mg/cm^3)	RT thermal conductivity (W/m·K)	Compressive strength (kPa)	Max service temperature (°C)	Ref.
$(Zr_{0.2}La_{0.2}Ce_{0.2}Hf_{0.2}Ho_{0.2}Er_{0.2})Si_{2.9}O_9$ fibrous aerogels	8.5	0.03–0.04	—	1300 (6 min)	[3]
SiC/SiO_2 nanofibrous aerogels	26.68–39.82	0.0208	15–160	1050	[9]
SiC nanofiber aerogel	9	0.029	18.72	900–950	[10]
Y/Yb doped SiO_2 aerogel	90–140	0.0287	—	1100 (42% shrinkage)	[56]
Graphene/SiC-nanosheets aerogel	10–30	0.025–0.035	5–16	850	[57]
BN@Al_2O_3 aerogel	—	0.076–0.104	—	1250	[58]
ABOw aerogel (this work)	173–243	0.0560–0.0873	97.8–214.3	1400–1500	—

different Al/B ratios maintained their shape well without collapse or deformation (Fig. 12(a)). The measured weight loss ranges from 14.1% to 21.2%, and the linear shrinkage ranges from 3.5% to 10.1% (Fig. 12(b)). Both values decrease with increasing Al/B ratios, indicating that a high boron content deteriorates the high-temperature resistance of the aerogel. XRD patterns (Fig. 12(d)) reveal that the samples with different Al/B ratios primarily contain $Al_{18}B_4O_{33}$. Compared with the presence of boric acid residue after calcination at 1000–1400 °C (Figs. 6(a)–6(c)), this indicates substantial volatilization of B_2O_3 during the holding process, which is the main reason for the weight loss of the samples. SEM images (Fig. 12(f)) show that the sample with an Al/B ratio of 2 : 1 still maintained a good whisker interconnection network structure. The whiskers are structurally intact, uniformly thick, and have a smooth surface, suggesting the potential of the areogel for long-term service at 1400 °C. In contrast, for the sample with an Al/B ratio of 1 : 1, the integrity and uniformity of the whisker structure within the matrix are acceptable; however, the whiskers on the fiber surface showed significant deformation, with blunted tips, non-uniform thickness, and localized sintering necks visible. For the sample with an Al/B ratio of 1 : 2, significant adhesion of whiskers is observed both within the matrix and on the fiber surfaces. The liquid phase between the whiskers is speculated to be primarily borosilicate, formed by the eutectic melting of free SiO_2 (generated from the decomposition of mullite fibers) and the residual B_2O_3 in the system.

After treatment at 1500 °C for 2 h, the ABOw aerogels with Al/B ratios of 1 : 1 and 2 : 1 remain structurally intact, while the sample with a ratio of 1 : 2 exhibits significant collapse and deformation, indicating complete failure (Fig. 12(a)). The weight loss of the samples ranges from 10.9% to 22.1%, and the sample with an Al/B ratio of 2 : 1 shows a linear shrinkage rate of only 4.1% (Fig. 12(c)). XRD analysis (Fig. 12(e)) reveals that the primary crystalline phase is $Al_{18}B_4O_{33}$, highlighting the excellent high-temperature resistance of the ABOw aerogel. SEM analysis (Fig. 12(g)) indicates that the thermal damage of the aerogel after treatment at 1500 °C is more severe than that at 1400 °C. The sample with an Al/B ratio of 2 : 1 exhibits the least structural damage: Whisker structures within the matrix are intact, while whiskers on the fiber surface show deformation and localized sintering necks. In the sample with an Al/B ratio of 1 : 1, noticeable adhesion of whiskers is observed both within the matrix and on the fiber surfaces. For the sample with an Al/B ratio of 1 : 2, a large amount of molten liquid phase is present. In summary, the high-temperature resistance of the samples is positively correlated with the Al/B ratio. The high-temperature failure process occurs sequentially as follows: excessive grain growth, whisker shape change, whisker adhesion, and finally melting. The ABOw aerogels with a high Al/B ratio can withstand prolonged use at 1400 °C and short-term exposure to 1500 °C.

High-temperature-resistant thermal insulation aerogels are of significant practical importance. In Table 3, the comprehensive properties of the ABOw aerogel developed in this study are compared with various high-temperature resistant aerogel systems reported in the literature. The results demonstrate that the ABOw aerogels possess an absolute advantage in terms of high-temperature resistance.

4 Conclusions

In this study, hierarchical ABOw aerogels were prepared using an aluminum–boron sol as the raw material, with chopped mullite fibers added as reinforcing agents and a secondary aluminum source. The synthesis involved a sol–gel process, followed by freeze-drying and a high-temperature *in-situ* reaction. The resulting structure features uniformly grown ABOw within the matrix, interspersed with either mullite fibers fully covered by ABOw (below 1200 °C) or rod-like assemblies of ABOw (above 1200 °C).

ABOw starts to form at 700 °C and undergoes a phase transformation from $Al_4B_2O_9$ to $Al_{18}B_4O_{33}$ between 1100 and 1200 °C. The growth of whiskers within the matrix is more significantly influenced by the Al/B ratios: Both the size of ABOw at each temperature and the phase transformation temperature decrease as the Al/B ratio increases. The ABOw diameter on the fiber surface is notably larger than that of ABOw within the matrix below 1200 °C. ABOw growth follows the V–S–L mechanism: Within the matrix, whiskers nucleate uniformly around alumina particles and then grow, with both diameter and aspect ratio increasing continuously; in contrast, whiskers on the fiber surface nucleate heterogeneously on preferentially oriented mullite grains, grow in clusters, and gradually merge into a single whisker of increasing length.

The density of the ABOw aerogel ranges from 0.173 to 0.243 g/cm^3, which decreases with increasing calcination temperature and decreasing Al/B ratio, influenced by the volatilization of B_2O_3. The thermal conductivity lies between 0.0560 and 0.0873 W/(m·K) and increases with increasing calcination temperature, mainly due to the reduced thermal resistance between whiskers resulting from grain growth, as well as enhanced gaseous conduction caused by increased pore size. The ABOw aerogels exhibit high strain tolerance, and the strength of samples calcined at 1200 °C ranges from 97.8 to 214.3 kPa. The strength at temperatures below 1200 °C increases with decreasing Al/B ratio and increasing calcination temperature; however, it decreases after treatment at 1400 °C, and the reduction extent diminishes as the Al/B ratio increases. The aerogel maintains phase stability after high-temperature heat treatment (1400 °C/20 h, 1500 °C/2 h), and its weight loss rate and linear shrinkage rate decrease with increasing Al/B ratio. The sample with an Al/B

ratio of 2 : 1 exhibits a linear shrinkage of less than 5% without an obvious welding phenomenon. This high-temperature resistant, lightweight, and thermally insulating ABOw aerogel is an excellent thermal protection material. Its unique pore structure also makes it suitable for high-temperature flue-gas filtration, adsorption, and catalysis.

Acknowledgements

This work is supported by the Fundamental Research Funds for the Central Universities (No. 3122025036).

Author contributions

Xin Tao: conceptualization, writing – original draft, project administration; Liangying Tang: methodology, software, data curation; Yuqi Zhao: formal analysis; Fangyu Zhao: resources, visualization; Ziwei Xiang: validation, methodology; Xinyue He: investigation; Mingchao Wang: supervision, funding acquisition.

Availability of data and materials

The data that support the findings of this study are available from the corresponding author upon reasonable request.

Competing interests

The authors have no competing interests to declare that are relevant to the content of this article.

Electronic Supplementary Material

Supplementary material is available in the online version of this article at https://doi.org/10.26599/JAC.2026.9221270.

References

[1] Guo JY, Chen JJ, Li JX, *et al.* Structural design of the multi-layer SiC nanofiber composite aerogel felt for applications in high-temperature thermal-insulating refractories. *J Eur Ceram Soc* 2025, **45**: 117370.

[2] Li Z, Chen ZK, Duan YM, *et al.* A review of silica aerogel based thermal insulation coatings: Preparation, properties and applications. *Prog Org Coat* 2025, **208**: 109449.

[3] Wang Y, Qin LY, Gong LL, *et al.* High-entropy ceramic nanofiber aerogel with excellent thermal stability for robust thermal insulation at high temperatures. *Ceram Int* 2025, **51**: 56804–56811.

[4] Zhang BJ, Duan JS, Wu AX, *et al.* Hierarchical porous Zr–SiC nanofibrous aerogels for advanced thermal insulation and electromagnetic wave absorption. *Chem Eng J* 2025, **524**: 169757.

[5] Yuan KK, Han DY, Liang JF, *et al.* Microwave induced *in-situ* formation of SiC nanowires on SiCNO ceramic aerogels with excellent electromagnetic wave absorption performance. *J Adv Ceram* 2021, **10**: 1140–1151.

[6] Yang WJ, Wei CX, Yuen ACY, *et al.* Fire-retarded nanocomposite aerogels for multifunctional applications: A review. *Compos Part B—Eng* 2022, **237**: 109866.

[7] Wang H, Huang Y, Liu SF, *et al.* A review of silica fiber-based aerogels: Composition, construction methods, mechanical enhancement strategies and applications. *Eur Polym J* 2024, **220**: 113367.

[8] Okafor PE, He CB, Tang GH. A critical review of superinsulation performance of ceramic nanofibrous aerogel for extreme conditions: Modeling, fabrication, applications, and outlook. *Adv Colloid Interf* 2025, **335**: 103352.

[9] Zhang P, Zhao S, Li KF, *et al.* Large-scale production of elastic SiC/SiO_2 nanofibrous composite aerogels with a labyrinth structure for high-temperature insulation, fire prevention, and noise absorption. *Chem Eng J* 2025, **505**: 159166.

[10] Song LM, Fan BB, Chen YQ, *et al.* Ultralight and hyperelastic SiC nanofiber aerogel spring for personal thermal energy regulation. *J Adv Ceram* 2022, **11**: 1235–1248.

[11] Hernández MF, López PV, Ferrari B, *et al.* Colloidal processing, sintering and properties of aluminum borate $Al_{18}B_4O_{33}$ porous ceramics. *Ceram Int* 2024, **50**: 1615–1622.

[12] Fu L, Deng MX, Lei ZH, *et al.* Insights into microstructure formation and thermal stability of aluminum borate whiskers: Effects of precursor powder. *J Am Ceram Soc* 2026, **109**: e70294.

[13] Pandey N, Chakrabarty I, Barkane K, *et al.* Microstructure, mechanical and wear properties of aluminum borate whisker reinforced aluminum matrix composites. *T Nonferr Metal Soc* 2020, **30**: 1731–1742.

[14] Luo H, Li YB, Xiang RF, *et al.* Novel aluminum borate foams with controllable structures as exquisite high-temperature thermal insulators. *J Eur Ceram Soc* 2020, **40**: 173–180.

[15] Xin JQ, Liu XE, He C, *et al.* Hierarchically porous aluminum borate whisker-based ceramics via freeze-gel casting and *in situ* reaction. *Prog Nat Sci—Mater* 2025, **35**: 333–338.

[16] Lao D, Zhang Y, Huang LF, *et al.* Microstructure, mechanical and neutron shielding properties of aluminum borate ceramics obtained from alumina and boric acid. *J Aust Ceram Soc* 2024, **60**: 905–915.

[17] Hernández MF, Suárez G, Cipollone M, *et al.* Formation, microstructure and properties of aluminum borate ceramics obtained from alumina and boric acid. *Ceram Int* 2017, **43**: 2188–2195.

[18] Liu XE, Dong X, Li X, *et al.* Aluminum borate whisker-based lattices with a hierarchical pore structure obtained via digital light processing. *Ceram Int* 2022, **48**: 23024–23032.

[19] Dong Y, Dong X, Li L, *et al.* Lightweight and thermally insulating aluminum borate nanofibrous porous ceramics. *Ceram Int* 2021, **47**: 21029–21037.

[20] Dong X, Sui GF, Guo AR, *et al.* Synthesis and properties of lightweight flexible insulant composites with a mullite fiber-based hierarchical heterostructure. *Chem Eng J* 2015, **277**: 159–167.

[21] Chen N, Wang HB, Huo JC, *et al.* Preparation and properties of *in-situ* mullite whiskers reinforced aluminum chromium phosphate wave-transparent ceramics. *J Eur Ceram Soc* 2017, **37**: 4793–4799.

[22] Zhao HJ, Wang JY, Xue JL, *et al. In situ* synthesised aluminium borate hollow whiskers reinforced aluminium phosphate wave-transparent ceramics. *Ceram Int* 2025, **51**: 24804–24812.

[23] Gökmen GG, Mishra YK, Akan T, *et al.* Nanostructured boron–aluminum–silicon (BAlSi) thin films: Synthesis via sol–gel and evaluation of antimicrobial efficacy. *Mater Sci Eng B—Adv* 2026, **324**: 119017.

[24] Wang SN, Liu H, Yuan S, *et al.* Sol–gel method on the preparation of boron-doped activated alumina. *IOP C Ser—Earth Env* 2021, **714**: 032057.

[25] Qiao XB, Cheng Y, Qin CX, *et al.* Preparation and spectral characteristics of Ce^{3+}-activated boroaluminate $LaAl_2B_3O_9$. *Appl Phys A* 2015, **118**: 749–756.

[26] Kuang HY, Pan YM, Tse JS. First-principles studies on the structure and B–O coordination of B_2O_3 glass at high pressure. *J Phys Chem C* 2024, **128**: 3543–3556.

[27] Furutani K, Ohkubo T, Du JC, *et al.* Elucidating the atomic structures of the gel layer formed during aluminoborosilicate glass dissolution: An integrated experimental and simulation study. *J Phys Chem C* 2022, **126**: 7999–8015.

[28] Przekop R, Kirszensztejn P. Porous xerogel systems B_2O_3–Al_2O_3 obtained by the sol–gel method. *J Non-Cryst Solids* 2014, **402**: 128–134.

[29] Kolet M, Atrash M, Molina K, *et al.* Sol–gel entrapped Lewis acids as catalysts for biodiesel production. *Molecules* 2020, **25**: 5936.

[30] Wang YF, Feng JC, Chen Z, *et al.* Wetting of microstructured alumina fabricated by epitaxial growth of $Al_4B_2O_9$ whiskers. *Appl Surf Sci* 2015, **357**: 766–770.

[31] Wang YF, Feng JC, Wang ZJ, *et al.* Joining of Al_2O_3 by epitaxial growth of aluminum borate whiskers for high-temperature applications. *Mater Lett* 2016, **163**: 231–235.

[32] Swamy V, Jung IH, Decterov SA. Thermodynamic modeling of the Al_2O_3–B_2O_3–SiO_2 system. *J Non-Cryst Solids* 2009, **355**: 1679–1686.
[33] Jia HB, Guo YL, Liu C. Transparent aluminoborosilicate glass-ceramics containing $Al_4B_2O_9$ nanorods. *Ceram Int* 2024, **50**: 29468–29475.
[34] Singh Gautam RK, Jha P, Gautam JK, *et al*. Synergetic study of Al_2O_3-boric acid in copper matrix: Aluminum borate formation and its effect on tribological characteristics of copper-based composites. *Wear* 2025, **578–579**: 206175.
[35] Liu YM, Li QQ, Fan SS. Self-catalytic growth of aluminum borate nanowires. *Chem Phys Lett* 2003, **375**: 632–635.
[36] Kenawy SH. Synthesis and characterization of aluminum borate ceramic whiskers. *Int J Appl Ceram Tec* 2011, **8**: 783–792.
[37] Song XL, Liu WS, Xu SH, *et al*. Microstructure and elastic modulus of electrospun Al_2O_3–SiO_2–B_2O_3 composite nanofibers with mullite-type structure prepared at elevated temperatures. *J Eur Ceram Soc* 2018, **38**: 201–210.
[38] Albarzan B, Almuqrin AH, Koubisy MS, *et al*. Effect of Fe_2O_3 doping on structural, FTIR and radiation shielding characteristics of aluminium–lead–borate glasses. *Prog Nucl Energ* 2021, **141**: 103931.
[39] Ahmed MR, Alsaif NAM, Siddiqui N, *et al*. Physical, thermal properties, FTIR and Raman spectroscopies as well as γ-ray attenuation capacity of borate glasses doped with Mn^{2+} ions: Role of CaO/Al_2O_3 substitution. *Opt Mater* 2025, **158**: 116461.
[40] Zhang CC, Gao XT, Yilmaz B. Development of FTIR spectroscopy methodology for characterization of boron species in FCC catalysts. *Catalysts* 2020, **10**: 1327.
[41] Ike PO, Nwanya AC, Agwu KK, *et al*. Structural, thermal and thermoluminescence response of transition and alkaline earth metals activated on aluminium borate $[Al_2(B_4O_7)_3$:Mn,Mg]. *Ceram Int* 2022, **48**: 15533–15540.
[42] Liu ZH, Tang J, Zhang LJ, *et al*. High-entropy ceramic aerogels for thermal insulation: Preparation, material systems, and compositional design strategies. *Chem Eng J* 2025, **525**: 169745.
[43] Song HS, Zhang J, Lin J, *et al*. Coating aluminum borate ($Al_{18}B_4O_{33}$) nanowire webs with BN. *J Phys Chem C* 2007, **111**: 1136–1139.
[44] Zhang MJ, Wang Y, Yu M, *et al*. Preparation of aluminum borate whiskers/$Co_xCr_{3-x}O_4$ catalysts on channel surface of cordierite honeycomb ceramic for soot catalytic combustion. *Int J Appl Ceram Tec* 2025, **22**: e14994.
[45] Škamat J, Lebedev A, Černašėjus O, *et al*. Effect of thermochemical boronizing of alumina surface on the borate crystals growth and interaction with nickel and nickel alloy. *Crystals* 2023, **13**: 4.
[46] Liu QY, Wang J, Liu ZX, *et al*. Water-tolerant boron-substituted MCM-41 for oxidative dehydrogenation of propane. *ACS Omega* 2022, **7**: 3083–3092.
[47] Fu ZY, Corker J, Papathanasiou T, *et al*. Critical review on the thermal conductivity modelling of silica aerogel composites. *J Build Eng* 2022, **57**: 104814.
[48] Zhu CY, Li ZY. Modeling of the apparent solid thermal conductivity of aerogel. *Int J Heat Mass Tran* 2018, **120**: 724–730.
[49] Berardi U, Nosrati RH. Long-term thermal conductivity of aerogel-enhanced insulating materials under different laboratory aging conditions. *Energy* 2018, **147**: 1188–1202.
[50] Tao X, Li JC, Liu JX, *et al*. Improved oxidation resistance and infrared emissivity of tantalum disilicide particles with sol–gel derived SiO_2 coatings. *J Alloy Compd* 2024, **971**: 172765.
[51] Jiang LN, Fan ZX, Guan JX, *et al*. Energy efficiency and carbon emission reduction of fly ash vacuum insulation boards: A coupled thermal modeling and lifecycle assessment. *J Clean Prod* 2026, **541**: 147471.
[52] Hou XB, Zhang RB, Fang DN. An ultralight silica-modified ZrO_2–SiO_2 aerogel composite with ultra-low thermal conductivity and enhanced mechanical strength. *Scripta Mater* 2018, **143**: 113–116.
[53] Huang T, Zhu Y, Zhu J, *et al*. Self-reinforcement of light, temperature-resistant silica nanofibrous aerogels with tunable mechanical properties. *Adv Fiber Mater* 2020, **2**: 338–347.
[54] Men J, He CB, Wang LK, *et al*. Synthesis of structure controllable carbon aerogel with low drying shrinkage and Scalable size as High-Temperature thermal insulator. *Chem Eng J* 2025, **503**: 157989.
[55] Chen CJ, Bai HZ, Bao HW, *et al*. The atomic structure evolution and strengthening mechanism in three-dimensional network graphene enhanced Cu: A molecular dynamics simulation. *J Alloy Compd* 2023, **963**: 171293.
[56] Wu SJ, Yu YX, Luo Z, *et al*. Enhancing particle heat resistance of the silicon–oxygen network skeleton in silica aerogel via Y/Yb dual-doping for thermal insulation. *Ceram Int* 2025, **51**: 22086–22102.
[57] Song LM, Chen YQ, Gao QC, *et al*. Low weight, low thermal Conductivity, and highly efficient electromagnetic wave absorption of three-dimensional graphene/SiC-nanosheets aerogel. *Compos Part A—Appl S* 2022, **158**: 106980.
[58] Song ZJ, Min ZY, Yuan HY, *et al*. Preparation and performance assessment of high wave-transmitting and high-temperature-resistant $BN@Al_2O_3$ aerogel for microwave sintering applications. *Ceram Int* 2026, **52**: 9453–9460.